Acta Materialia 195 (2020) 184–198

Contents lists available at ScienceDirect

Acta Materialia

journal homepage: www.elsevier.com/locate/actamat

High pressure torsion of Cu–Ag and Cu–Sn alloys: Limits for solubility and dissolution

B.B. Straumal[a,b,c,*], A.R. Kilmametov[a,b], B. Baretzky[b], O.A. Kogtenkova[a], P.B. Straumal[c,d], L. Lityńska-Dobrzyńska[e], R. Chulist[e], A. Korneva[e], P. Zięba[e]

[a] Institute of Solid State Physics and Chernogolovka Scientific Center, Russian Academy of Sciences, Ac. Ossipyan str. 2, Chernogolovka, 142432 Russia
[b] Institute of Nanotechnology, Karlsruhe Institute of Technology, Hermann-von-Helmholtz-Platz 1, 76344 Eggenstein-Leopoldshafen, Germany
[c] National University of Science and Technology «MISIS», Leninskii prosp. 4, 119049 Moscow, Russia
[d] Institute of Metallurgy and Materials Science, Russian Academy of Sciences, Leninsky prospect 49, 117991 Moscow, Russia
[e] Institute of Metallurgy and Materials Science, Polish Academy of Sciences, Reymonta St. 25, 30-059 Cracow, Poland

ARTICLE INFO

Article History:
Received 4 April 2020
Revised 20 May 2020
Accepted 25 May 2020
Available online 29 May 2020

Keywords:
Nano-crystalline metals
Cu-based alloys
High-pressure torsion
Solubility
Dissolution

ABSTRACT

The high-pressure torsion (HPT) of binary copper alloys with 3, 5, 8, 10 wt. % Ag and 14 wt. % Sn has been studied at room temperature T_{HPT}. Before HPT, the Cu–Ag alloys have been annealed at 12 different temperatures between 320 and 800 °C and Cu–14 wt. % Sn has been annealed at 9 different temperatures between 310 and 500 °C. Thus, before HPT the Cu–Ag alloys consisted of Ag-particles in the Cu-based matrix with silver content c_{init} from almost zero to 8 wt.%. The Cu–14 wt. % Sn samples had Cu-based matrix with tin concentration c_{init} from almost zero to 14 wt.% Sn and precipitates of ε or δ Hume-Rothery intermetallic phases. After about 1.5 plunger rotations a certain steady-state concentration c_{ss} of the alloying element is reached in the matrix. The measured c_{ss} values were 5.5±0.1 wt. % Ag and 13.1±0.1 wt. % Sn. If the initial concentration c_{init} in Cu matrix was below c_{ss} ($c_{init} < c_{ss}$), it increased towards c_{ss} during HPT. If $c_{init} > c_{ss}$ it decreased towards c_{ss}. We observed that c_{ss} did not depend on c_{init} in broad interval of c_{init} and was, therefore, equifinal. The equifinal c_{ss} values corresponded to the certain equilibrium solubilities of silver and tin in Cu matrix and allowed to estimate the (elevated) effective temperature as T_{eff} (Ag) = 700±10 °C and T_{eff} (Sn) = 400±10 °C, respectively. The observed phenomena are discussed using the ideas of non-equilibrium thermodynamics of open systems. During HPT the decomposition of a solid solution competed with dissolution of precipitates. As a result, a dynamic equilibrium established between precipitation and dissolution at steady-state deformation stage. In this dynamic equilibrium a certain steady-state concentration c_{ss} of the alloying element is reached in the matrix. In Cu-based alloys, the obtained T_{eff} is always higher than T_{HPT} and correlates with activation enthalpy of dopant diffusion in Cu. Other HPT-driven phenomena such as accelerated mass transfer, intermetallic phase formation, grain boundary faceting and grain boundary segregation are taken into account to evaluate the effective temperature T_{eff}.

1. Introduction

Generally, during high-pressure torsion (HPT) the decomposition of a solid solution very often competes with dissolution of the secondary phase precipitates [1–5]. As a result, a dynamic equilibrium between these two processes is established, and a certain steady-state (or stationary) concentration c_{ss} of alloying element in the matrix is reached [4]. In order to understand the peculiarities of this process, we would like to apply the ideas of thermodynamics of non-equilibrium processes [6–9].

In closed systems (i.e. those well separated from the environment) the equilibrium state can be reached. For certain values of external parameters (like temperature, pressure, magnetic field etc.) only one equilibrium state exists and corresponds to the minimum of free enthalpy (or maximum of entropy) [6]. In the multicomponent and multiphase systems the equilibrium state is described by a certain amount of each phase and certain composition of them. The variety of equilibrium states at different temperatures, pressures, compositions etc. is described by the equilibrium phase diagrams [10]. If we slightly change the temperature or pressure, the initial equilibrium state becomes non-equilibrium, and the driving force appears which moves the system towards the new equilibrium [6,8]. Thus, the true thermodynamic equilibrium state does not depend on the initial state. It should only correspond to the minimum of free enthalpy.

* Corresponding author at: Institute of Solid State Physics, Russian Academy of Sciences, Chernogolovka, Moscow district 142432 Russia.
E-mail addresses: straumal@issp.ac.ru, straumal@mf.mpg.de (B.B. Straumal).

https://doi.org/10.1016/j.actamat.2020.05.055
1359-6454/

If a system is not closed and a certain energy flux from outside to or through the system exists, the system becomes non-equilibrium. In order to describe such systems we should use the instruments of non-equilibrium thermodynamics [7,8]. If the deviation from equilibrium is small, the linear non-equilibrium thermodynamics is applicable [6]. If the deviation from equilibrium is large, the instruments of non-linear non-equilibrium thermodynamics should be used [8,9]. In the case of small deviation from equilibrium, one still can use the equilibrium phase diagrams and the (stable and metastable) phases from these diagrams [10]. In the case of large deviation from equilibrium, new (so called dissipative) structures can arise. The dissipative structures cannot be anymore described with equilibrium phase diagrams [8,9]. The most famous dissipative structures are the so-called Bénard cells which appear by increase of thermal gradient and transition from conductive to convective heat conduction or Belousov-Zhabotinsky reaction with oscillations [8,9].

The processes of severe plastic deformation (SPD), in particular of high pressure torsion are strongly non-equilibrium [11]. Therefore, the approach and ideas of non-equilibrium thermodynamics should be used for the description of SPD-driven phenomena. In particular, if the external conditions (like the energy flux through the system) are stable, the certain stationary state (called also steady-state) establishes in the open system. The condition of its existence is the lowest entropy production (instead of minimum free enthalpy for equilibrium ones) [7]. Such stationary state is sustainable. It means that if the small deviation appears from the stationary state (and the entropy production deviates from the minimum), the driving force arises which moves the system back towards the stationary state [6,7]. In this case such stationary state is called equifinal [12], because it does not depend on the starting state. From this point of view, the *equifinality* for stationary states in open systems is similar to the *equilibrium* for the closed systems.

The HPT-driven competition between decomposition of supersaturated solution and dissolution of precipitates is the good example of such equifinal processes. During HPT, after a certain transition stage (about 1–1.5 revolutions of HPT anvils), the dynamic equilibrium appears between decomposition of supersaturated solution and dissolution of precipitates [13]. In this dynamic equilibrium a certain steady-state concentration of alloying element c_{ss} in solid solution establishes. The concentration c_{ss} is *equifinal*, in other words it does not depend on the initial state before HPT. If the initial concentration in a solid solution c_{init} is lower than c_{ss} i.e. $c_{init} < c_{ss}$, it increases towards c_{ss} during HPT. If the initial concentration in a solid solution c_{init} is higher than c_{ss} i.e. $c_{init} > c_{ss}$, it decreases towards c_{ss} during HPT. This phenomenon we observed in the Cu–Co, Cu–Ag and Cu–Sn systems [2,3,5]. We annealed the Cu–Co, Cu–Ag and Cu–Sn samples at two temperatures in such a way that in one sample $c_{init} < c_{ss}$ and in other $c_{init}) c_{ss}$. And indeed, during HPT in the first case c_{init} increased and reached c_{ss}, and in second case c_{init} decreased and reached c_{ss} [2,3,5]. Thus, c_{ss} plays a role of a certain attractor [9] for HPT of diluted copper-based alloys. It means that, due to the equifinality, the c_{ss} point "attracts" the system during HPT if initial concentration c_{init} in a solid solution differs from c_{ss}. However, the thermodynamics of non-equlibrium processes predicts that each attractor has a certain sustainability area in a phase space from which the points are moving towards it. Other attractors have different areas separated by energetic mountains (ridges) maybe with saddles [8,9]. In our previous experiments the $c_{init} < c_{ss}$ and $c_{init} > c_{ss}$ values were not far away from c_{ss} [2,3,5]. Thus, the question arises, how broad is the sustainability area of each attracting c_{ss} point? Can we reach its boundaries? Can we find another attractor(s)? In order to answer these questions, we annealed the Cu–Ag and Cu–Sn alloys in the broad interval of temperatures in order to get the interval of c_{init} values as broad as possible and subjected them to the HPT treatment.

2. Experimental

The copper alloys with 3, 5, 8, 10 wt. % Ag and 14 wt. % Sn in the form of cylindrical ingots, have been prepared from the high-purity 5N8 Cu, 5 N Ag and 5N3 Sn by the vacuum induction melting. For the HPT processing, the 0.6 mm thick disks were cut from the as-cast ingots, then ground and chemically etched. They were sealed into evacuated silica ampoules with a residual pressure of approximately 4×10^{-4} Pa at the room temperature. The annealing temperatures and durations were given in Table 1. The annealed samples were HPT-processed at room temperature for five full plunger revolutions at a constant rotation speed of one rotation per minute and a pressure of 6 GPa using a custom built computer controlled HPT device (W. Klement GmbH, Lang, Austria). An equal construction of the anvils was used to produce all the HPT-samples of 0.35 mm in thickness.

Torsion straining of a disc sample of diameter *2R* and thickness *t* produces a shear strain γ:

$$\gamma = 2\pi\, n\, r/t \tag{1}$$

n being the number of rotations of the mobile anvil, *r* being the distance from the sample centre. γ varies from zero on the sample axis to a maximum value γ_{max} on the lateral surface (situated at a distance $r = R$ from the axis). For comparison of shear deformation with tensile strain, the equivalent strain value e_{eq} can be used [14,15]:

$$e_{eq} = \gamma/\sqrt{3} = 2\pi nr/t\sqrt{3} \tag{2}$$

All samples for the investigations were cut from the deformed disks at a distance of r = 3 mm from the sample centre. For this distance and 5 anvil rotations γ = 270 and e_{eq} = 156, respectively. This strain value has been typically used for the production of nanograined materials in earlier studies [1,14,15]. The strain rate for γ is about 0.9 s^{-1} and for e_{eq} it is about 0.5 s^{-1}. It follows from the Eqs. (1) and (2) that a certain strain gradient exists in HPT samples. Therefore, the samples for the microstructure studies were cut from the HPT-processed disks at a distance of R = 3 mm from the sample centre. For the metallographic investigations the samples were ground with SiC grinding paper, and sequentially polished with 6, 3, and 1 μm diamond pastes. The prior inspection of obtained material was carried out on a Dual beam high-resolution Scanning Electron Microscopy (SEM) FEI Quanta 3D FEGSEM integrated with the EDAX Trident system for an energy dispersive X-ray (EDX) microanalysis. The details of microstructure were studied using a TECNAI G2 FEG super TWIN (200 kV) transmission electron microscope (TEM) equipped with the

Table 1
The annealing temperatures *T* and durations *t* for Cu–Ag and Cu–Sn alloys.

Cu–Ag alloys												
T, °C	320	380	400	500	600	620	650	700	750	780	790	800
t, h	1200	1200	1200	710	770	450	100	100	200	290	300	300
Cu–Sn alloys												
T, °C	310	320	330	365	370	400	430	500	570			
t, h	1702	1200	910	1025	715	888	600	894	288			

EDX spectrometer manufactured by EDAX. The thin foils for TEM observation were prepared by a twin-jet polishing technique using an electrolyte D2 manufactured by Struers company. The X-ray diffraction (XRD) patterns were obtained in the Bragg–Brentano geometry in a powder diffractometer (Philips X'Pert) with Cu-Kα radiation. The Pseudo-Voigt function was used for fitting of XRD peak profiles. Lattice parameters were evaluated by the Fityk software [16] using a Rietveld-like whole profile refinement. An empirical rule known as Vegard's rule (1921) was taken into account for subsequent analysis of solid solutions. The phase analysis was also made by high energy synchrotron radiation and a 2D detector using P07B line in DESY, Hamburg, Germany. The wave length was 0.014235 nm (87.1 KeV). The use of such an energy allowed experiments in transmission mode resulting in much better grain statistic compared to the conventional X-ray diffraction.

3. Results

According to Table 1, a number of alloys attributed to Cu-based solid solutions of the Cu–Ag and Cu–Sn systems were treated by annealing and subsequent quenching into ice-water in order to perform a wide range of different initial compositions. These treatments led to various concentrations of Ag and Sn in the (Cu) matrix and to the secondary phase precipitations. Some initial states contained (Cu) solid solution only. In Fig. 1 the Cu-rich parts of Cu–Ag (a) and Cu–Sn (b) phase diagrams are presented [10]. The squares show the annealing temperatures and concentrations in alloys before (solid ones) and after HPT (open ones). The arrows show how the composition of (Cu) matrix changed during HPT. The vertical dashed lines are for the c_{ss} steady state concentrations in Cu–Ag (a) and Cu–Sn (b) alloys.

SEM micrographs of various Cu–Ag alloys are shown in Fig. 2. Fig. 2a presents the microstructure of the Cu–8 wt.% Ag alloy annealed at 500 °C for 710 h as the initial state before HPT. The (Cu) solid solution matrix appears as dark background for the Ag precipitates, which are visible as bright spots. The grain size in (Cu) matrix is about dozens of micrometers. The (Cu) grains are slightly elongated perpendicular to the ingot axis. Two kinds of Ag precipitates can be distinguished. The bigger ones of about 3-4 μm are located mainly in the (Cu)/(Cu) grain boundaries (GBs) and GB triple junctions (TJs). The fine Ag precipitates of about 50-10 nm are mainly inside of the (Cu) grains, but they also form chains along the (Cu)/(Cu) GBs. Fig. 2b shows the Cu–8 wt.% Ag alloy annealed at 500 °C for 710 h after HPT. The (Ag) precipitates are transformed into broad bands with fuzzy borders. These broad bands fill the volume of the specimen almost uniformly. They consist of small individual particles that cannot be resolved in SEM images.

The initial state of Cu–8 wt.% Ag alloy annealed at 600 °C for 770 h is shown in Fig. 2c. The grain size in (Cu) matrix is about 10-20 μm. The (Cu) grains seem to be equiaxial. Only large silver precipitates are visible. Their size is 1-5 μm, and they are also located mainly in the (Cu)/(Cu) GBs and TJs. However, they are more equiaxial than in Fig. 2a. The fine Ag precipitates which could be visible in SEM micrographs (Fig. 2a) are absent. Fig. 2d shows the Cu–8 wt.% Ag alloy annealed at 600 °C for 770 h after HPT. The (Ag) precipitates are also transformed into broad bands with fuzzy borders. However, their morphology differs from those in Fig. 2b. One can observe here how the individual (Ag) precipitates are fragmented during HPT.

Fig. 2e shows the Cu–8 wt.% Ag alloy annealed at 780 °C for 290 h. The (Cu) grains have a size of about 500 μm and they are free from Ag precipitates. However, the narrow bands of discontinuous precipitates [17] exist along the (Cu)/(Cu). They are well visible in GB TJ (Fig. 2f). Fig. 2g shows the Cu–10 wt.% Ag alloy annealed at 780 °C for 290 h. This alloy contains more silver than previous one. Therefore, it solidified at the eutectic temperature T_e during the cooling. Just above T_e the (Cu)/(Cu) GBs are (completely or partially) wetted by the Ag-rich melt. Thus, the (Cu) grains have a size of about 200-500 μm and are free from Ag precipitates. The (Cu) grains are surrounded by the Ag-rich layers transformed into (Cu)+(Ag) mixture with typical eutectic structure good visible in GB TJ (Fig. 2h).

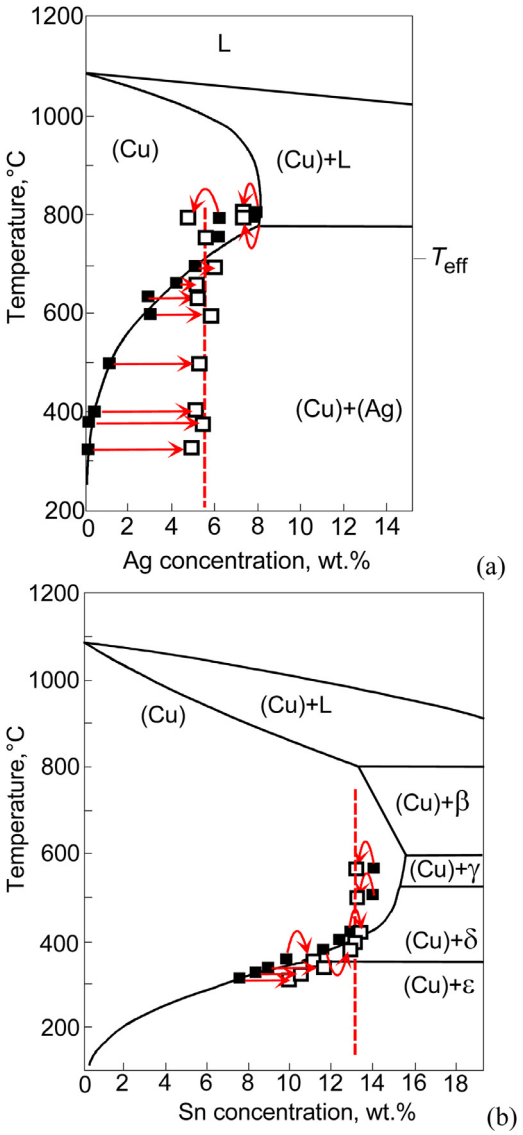

Fig. 1. Cu-rich parts of Cu–Ag (a) and Cu–Sn (b) phase diagrams [10]. The squares show the annealing temperatures and concentrations in alloys. Solid squares show the composition in the matrix (Cu) solid solution before HPT. Open squares show the composition in the matrix (Cu) solid solution after HPT. The arrows show how the composition of (Cu) matrix changes during HPT. The vertical dashed lines show the c_{ss} steady state concentrations in Cu–Ag (a) and Cu–Sn alloys.

In Fig. 3 the bright field (a, d, g, j) and dark field (b, e, h, k) TEM micrographs with selected area electron diffraction pattern (c, f, i, l) are shown for the Cu–8 wt.%Ag (a-i) and Cu–10 wt.%Ag (j-l) alloys after HPT deformation at 500 °C (a–c), 600 °C (d–f) and 780 °C (g-l). In all samples the copper grains are strongly refined after HPT, and their size is about 100–200 nm. The silver rings in the diffraction pattern for Cu–8 wt.%Ag samples (Fig. 3 a-i) after HPT are very weak, and respective Ag particles are hardly visible. Only in the Cu–10 wt.%Ag sample (Fig. 3 g-l) the strongest silver rings in the diffraction pattern are visible and silver particles are also visible as white spots in the bright field image (Fig. 3j). The size of these silver particles is about 20-50 nm.

Synchrotron XRD patterns of Cu–8 wt.% Ag alloy before (a, c, e) and after HPT deformation (b, d, f), previously annealed at 500 °C (a, b), 600 °C (c, d) and 800 °C (e, f), are displayed in Fig. 4. The number

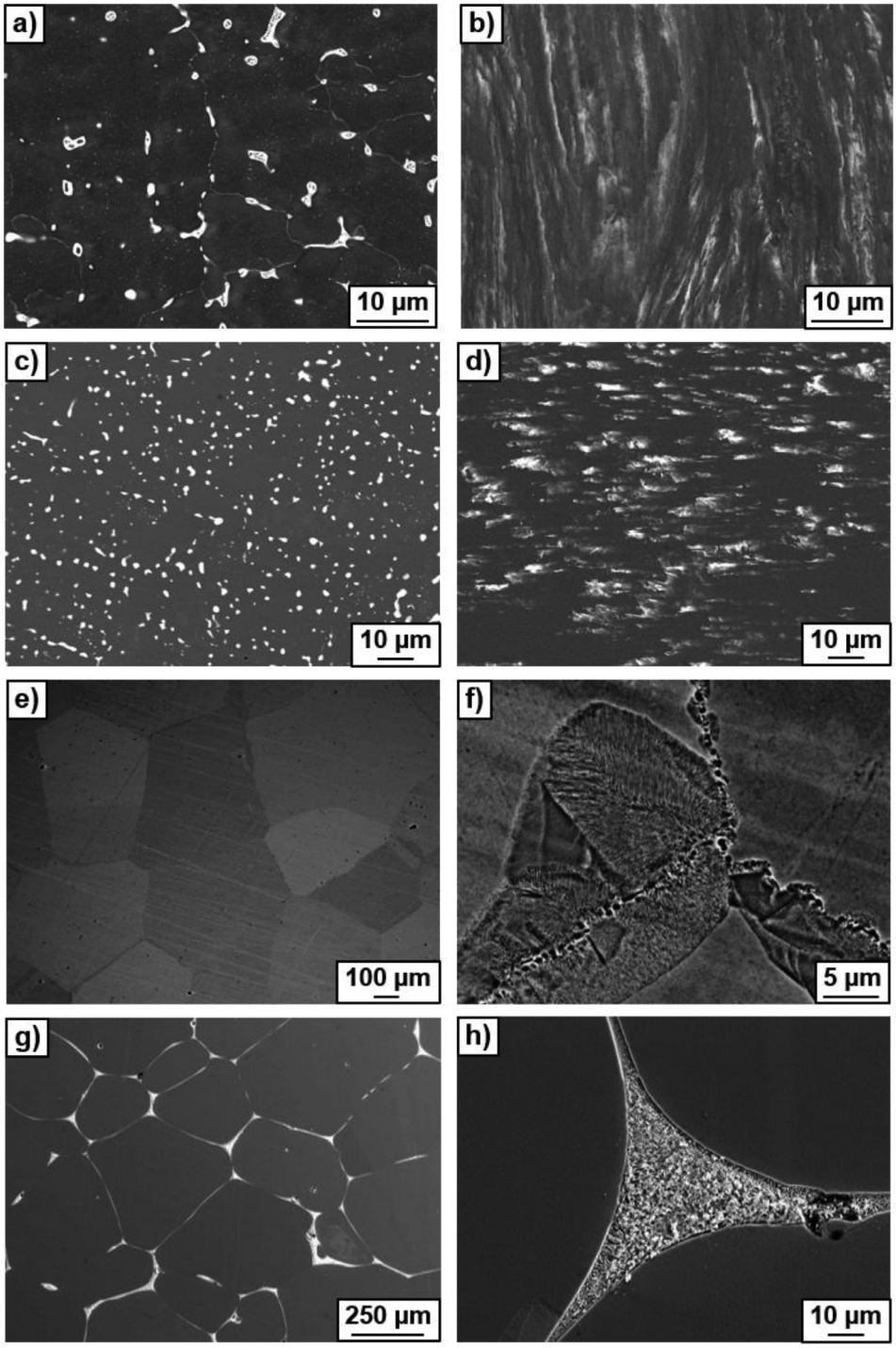

Fig. 2. SEM micrographs of Cu–Ag alloys. (a, b) Cu–8 wt. %Ag alloy annealed at 500 °C for 710 h before (a) and after (b) HPT. (c, d) Cu–8 wt. %Ag alloy annealed at 600 °C for 770 h before (b) and after (d) HPT. (e, f) Cu–8 wt. %Ag alloy annealed at 780 °C for 290 h. (f) the magnified view of GB TJ from Fig. 2e. (g, h) Cu–10 wt. %Ag (e) alloy annealed at 780 °C for 290 h. (h) the magnified view of GB TJ from Fig. 2g.

of individual spots at XRD rings of annealed samples (Figs. 4 a,c,e) decreases with increasing annealing temperature. It means that the size of copper grains in the annealed samples increases with increasing temperature from 500 to 800 °C. The silver rings are absent in Fig. 4f, though silver rings are visible in the comparable selected area electron diffraction patterns in Fig. 3i. The explanation of that is that the sensitivity of SAED in TEM is higher than that of X-rays or even synchrotron diffraction. In the HPT-treated samples all XRD rings become almost continuous; the individual spots are not more resolvable. The rings themselves become broader. It means that HPT leads to the strong grain refinement. In Fig. 5, the synchrotron XRD patterns are compared for the copper alloys with 3 (a), 5 (b), 8 (c) and 10 wt. % Ag (d) annealed at the same temperature of 800 °C. Silver rings are absent in the Figs. 5 a,b,c. They are present in Fig. 5d, i.e. only in the sample with 10 wt. % Ag. In Fig. 6 the synchrotron XRD pattern is presented for the 10 wt. % Ag alloy annealed at 800 °C and HPT treated after annealing. In comparison to Fig. 5d, all XRD rings become almost continous after HPT; the individual spots are not resolvable anymore, and diffraction rings of silver appeared to be clearly visible.

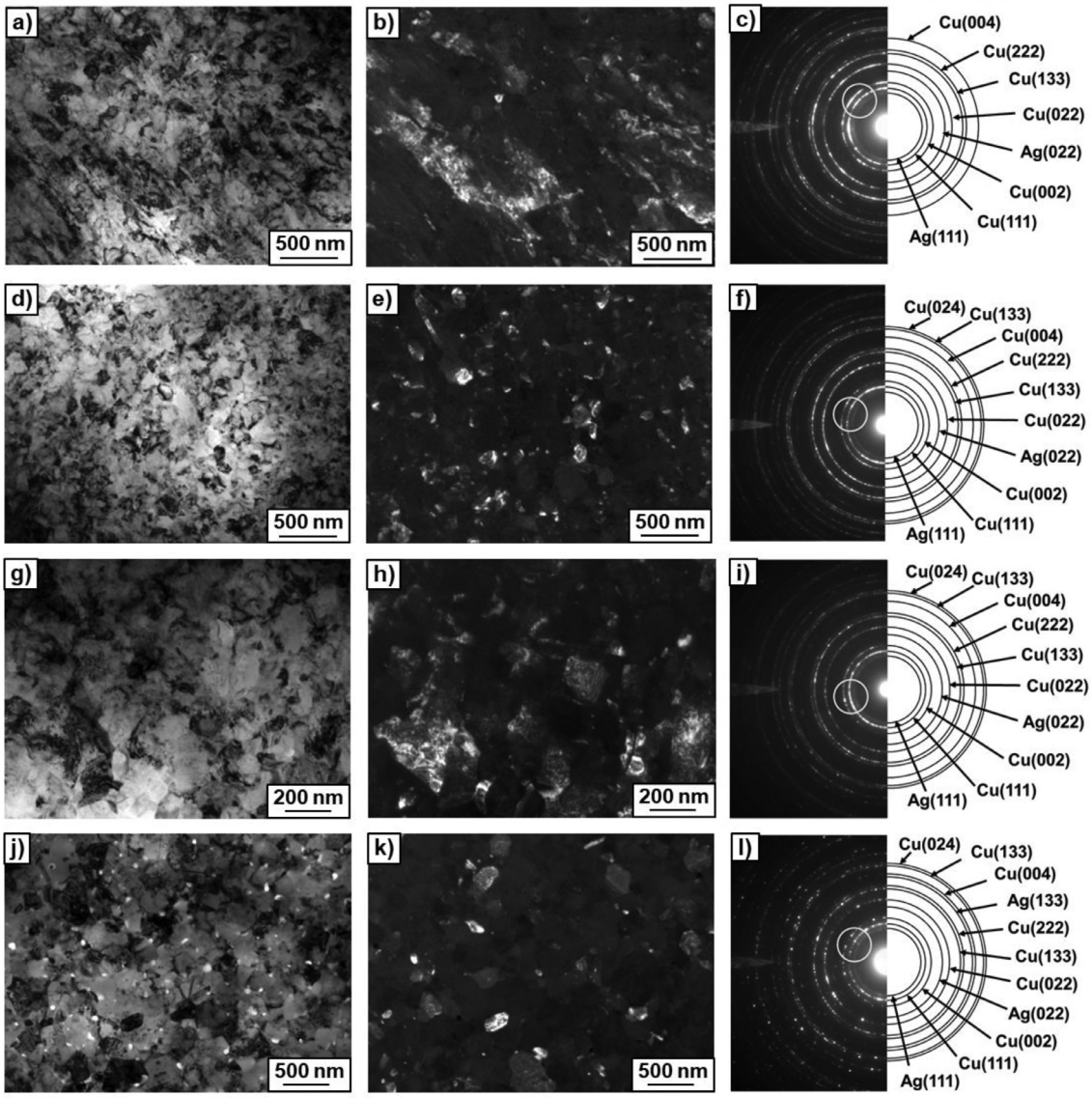

Fig. 3. Bright field (a, d, g, j) and dark fields (b, e, h, k) TEM micrographs with selected area electron diffraction patterns (c, f, i, l) for the Cu–wt. 8% Ag alloy (a-i) and Cu–wt. 10% Ag alloy (j-l) after HPT deformation, previously annealed at 500 °C (a-c), 600 °C (d-f) and 780 °C (g-l). The position of the objective aperture for the respective dark field images is marked by a white circle.

In Fig. 7, the XRD patterns obtained using conventional diffractometer are shown for the copper alloy with 8 wt. % Ag after annealing and following HPT. For the Cu–8 wt. % Ag alloy annealed at 500 °C the XRD peaks of copper shift to the left (i.e. towards lower diffraction angles) after HPT. For the Cu–8 wt. % Ag alloy annealed at 790 °C the XRD peaks of copper shift to the right (i.e. towards higher diffraction angles) after HPT.

Dependences of the lattice parameter in the (Cu) matrix solid solution of Cu–Ag alloys on the annealing temperature before and after HPT are presented in Fig. 8. The solid squares present the concentration in (Cu) after annealing before HPT, while the open squares correspond to the concentration in the (Cu) matrix solid solution after annealing and HPT deformation. Further, the red arrows show how the concentration of Ag in (Cu) matrix changes after HPT. Finally, the grey square indicates the lattice parameter value in pure copper. As one can see from Fig. 8, a certain steady-state lattice parameter is about 0.3634 nm. If the lattice parameter in (Cu) solid solution before HPT is below than 0.3634 nm, the HPT leads to the increase of (Cu) lattice parameter, i.e. to the increase of silver content in (Cu) matrix. Correspondingly, if the lattice parameter in (Cu) solid solution before HPT is higher than 0.3634 nm, the HPT leads to its decrease, i.e. to the decrease of silver content in (Cu). However, the lattice parameter reaches the 0.3634 nm value not for all the samples after HPT, but indicates the samples that undergo either decomposition or enrichment of (Cu) solid solution.

SEM micrographs of Cu–14 wt. % Sn alloy annealed at 320 °C for 1200 h before (a) and after (b) HPT are presented in Fig. 9. In accordance with Cu–Sn phase diagram (Fig. 1, [10], the sample contains the Cu-based α solid solution (appears as dark in the micrographs) and ε intermetallic phase (appears as bright in the micrographs). The ε intermetallic phase is quite hard, and HPT did not lead to its significant fragmentation. However, the coarse particles of ε-phase are surrounded by the α-phase border which appears lighter than the α areas which are far away from ε-phase. This is a sign of a certain dissolution of some tin atoms in the α-phase teared off the ε-phase. The SEM micrographs of Cu–14 wt. %Sn alloy annealed at 370 °C for 715 h before (a) and after (b) HPT are shown in Fig. 10. They are quite similar to those in Fig. 9. Namely, the sample also contains the Cu-based α solid solution (appears as dark in the micrographs) and ε intermetallic phase (appears as bright in the micrographs). Also, the

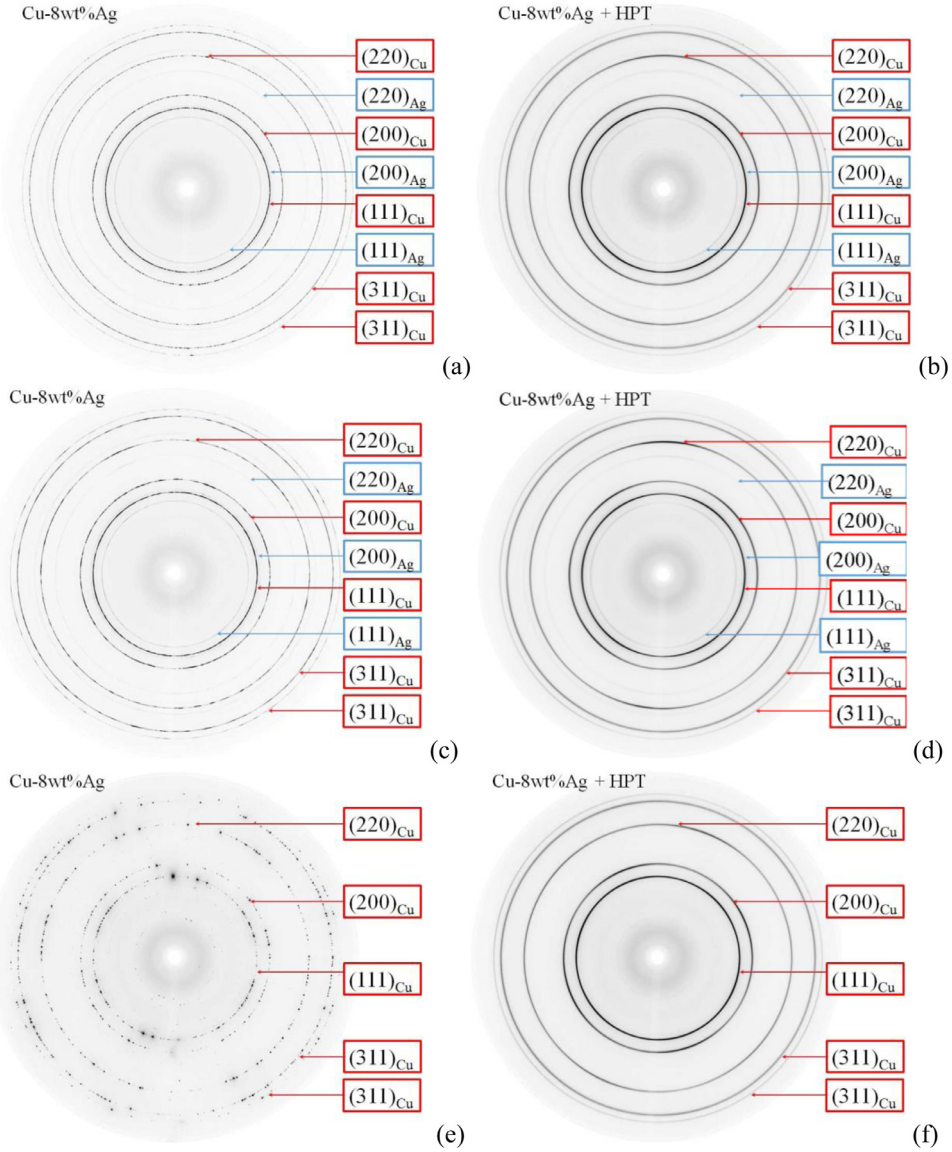

Fig. 4. Synchrotron X-ray diffraction patterns of Cu–8 wt. % Ag alloy before (a, c, e) and after HPT deformation (b, d, f), previously annealed at 500 °C (a, b), 600 °C (c, d) and 800 °C (e, f).

coarse particles of ε-phase after HPT are surrounded by the α border which appears lighter than the α areas and contain more tin than the darker areas which are far away from ε-phase. In Fig. 11, the SEM micrographs of Cu–14 wt. % Sn alloy annealed at 500 °C for 894 h before (a) and after (b) HPT are shown. In accordance with Cu–Sn phase diagram (Fig. 1, [10]), the sample before and after HPT contains only the Cu-based α solid solution.

In Fig. 12, the bright field (a) TEM micrograph and selected area electron diffraction patterns (b, c) of Cu–14 wt. % Sn alloy after HPT deformation, previously annealed at 320 °C for 1200 h are demonstrated. Fig. 12a witnesses that the grain size in the Cu-based solid solution (α-phase) strongly decreased. The electron diffraction patterns (Figs. 12b,c) show that the sample after HPT indeed contains the α- and ε-phases. Bright field (a) and dark field (b) TEM micrographs with electron diffraction pattern (c) of Cu–14 wt. % Sn alloy after HPT deformation, previously annealed at 500 °C for 894 h, are shown in Fig. 13. The grain size in the Cu-based solid solution (α-phase) also strongly decreased after HPT and estimated to be about 200 nm. The electron diffraction pattern (Figs. 13c) shows that the sample after HPT contains only α-phase.

The XRD patterns obtained with diffractometer are shown (Fig. 14) for the copper alloy with 14 wt. % Sn after annealing at 320 and 500 °C and subsequent HPT. For the Cu – 14 wt. % Sn alloy annealed at 320 °C, the XRD peaks of copper shift to the left (i.e. towards lower diffraction angles) after HPT. For the Cu – 14 wt. % Sn alloy annealed at 590 °C the XRD peaks of copper shift to the right (i. e. towards higher diffraction angles) after HPT. Fig. 15 represents the changes in lattice parameter values for (Cu) matrix solid solution of Cu–14 wt. % Sn alloy before and after HPT. The solid squares show the concentration in (Cu) after annealing before HPT while the open squares the concentration in (Cu) matrix solid solution after annealing and HPT. On the other hand, the red arrows show how the concentration of Sn in (Cu) matrix changes after HPT. As one can see, a certain value of lattice parameter approaches to about 0.3693 nm (shown by the vertical dotted red line). If the lattice parameter in (Cu) solid solution before HPT is below than 0.3693 nm, the HPT leads to the increase of (Cu) lattice parameter, i.e. to the increase of tin content in (Cu). Correspondingly, if the lattice parameter in (Cu) solid solution before HPT is higher than 0.3693 nm, HPT leads to its decrease, i.e. to the decrease of tin content in (Cu). However, the

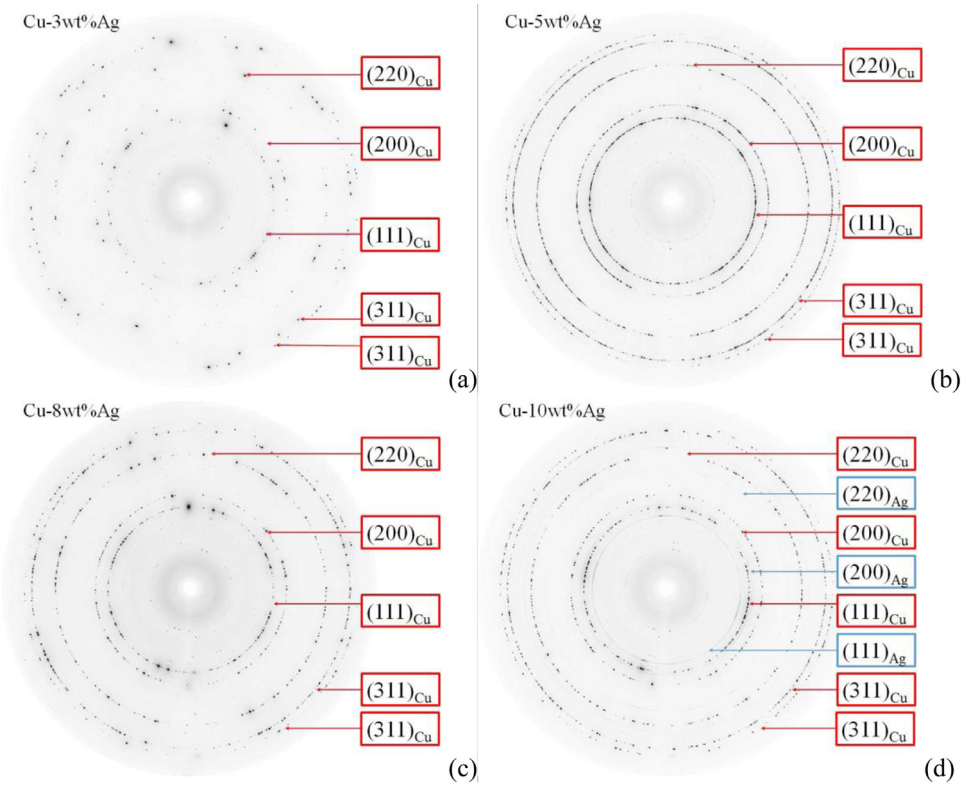

Fig. 5. Synchrotron X-ray diffraction patterns of Cu-based alloys with 3 (a), 5 (b), 8 (c) and 10 wt. % Ag annealed at 800 °C.

lattice parameter reaches the value of 0.3693 nm not for all the states after HPT, but this meaning indicates the states of Cu-Sn alloy where either decomposition or enrichment of (Cu) solid solution takes place.

4. Discussion

4.1. Grain size and hardness in HPT stationary state (steady-state)

As it well known, methods of SPD allow to achieve extremely high values of accumulated strain during refinement of the structure. HPT technique implies that under conditions of applied pressure the given sample can be deformed without break and nearly retains its original shape. In general, the shape of the disk between two HPT anvils remains unchanged even after dozens anvil rotations. Indeed, the HPT can continue until the break of anvils (from ~20 rotations for hard Nd-Fe-B alloys [18,19] up to hundreds or even thousands anvil rotations for the soft Al-, Mg- or Cu-based alloys [20–24]). With the beginning of HPT processing, the amount of lattice defects increases. One cannot expect that the concentration of defects (such as vacancies, dislocations or grain boundaries) would continuously grow up with the increasing number of anvil rotations. Taking into account that HPT mostly proceeds at ambient conditions, the relaxation starts even if HPT takes place at room temperature T_{HPT}. In this case, the coefficients of conventional bulk diffusion at T_{HPT} are below 10^{-30}–10^{-40} m^2/s. The relaxation accelerates until its rate becomes equal to the rate of defects production and dynamic equilibrium establishes. One has to underline that usually the samples are almost

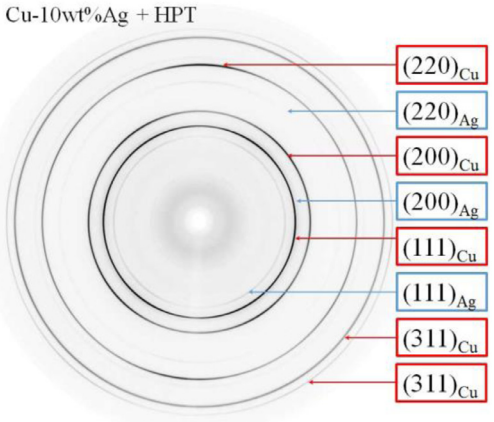

Fig. 6. Synchrotron X-ray diffraction pattern of Cu 10 wt. % Ag alloy after HPT deformation previously annealed at 800 °C.

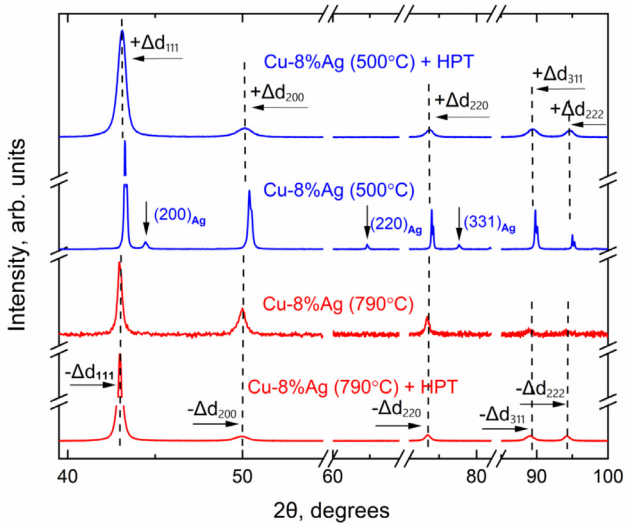

Fig. 7. X-ray diffraction pattern of Cu – 8 wt. % Ag alloy before and after HPT deformation previously annealed at 500 and 790 °C.

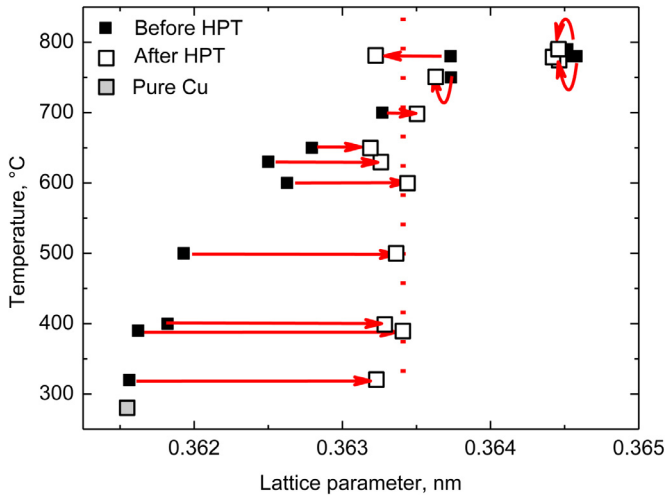

Fig. 8. Plots showing the dependence of lattice parameter in the (Cu) matrix solid solution of Cu–Ag alloys on the annealing temperature before and after HPT. The solid squares are for the concentration in (Cu) after annealing before HPT. The open squares show the concentration in the (Cu) matrix solid solution after annealing and HPT. Red arrows indicate how the concentration in (Cu) changes after HPT. Grey square denotes the lattice parameter in pure copper. Vertical dotted line shows the concentration c_{ss}.

not heated during HPT at ambient room temperature [25,26] and stay just a little bit warm [27,28].

Therefore, the steady-state deformation is reached after some number of anvil rotations [2,4,29]. For example, in the case of Al-, Cu-, Mg- or even Ti-based alloys the torsion torque increases during first 1–1.5 rotations and then saturates [2,4,24,27,30]. If the material is hard, like for example the Nd-Fe-B alloys, the torsion torque saturates later [4,18,19]. In the steady state, other characteristics are also tending to saturation like, for example, the grain size value. The SPD-driven grain refinement is the well-known process [11,24,31–35]. During SPD of coarse-grained pure metals, the grain size decreases down to a few hundreds of nanometers, reaches its steady-state value, and does not decrease further [28,36–39]. The steady-state grain size is determined for different SPD techniques [4]. In case of copper it is minimal for ball milling (BM) [40], slightly higher for HPT [2,41–43] and further increases for planar twist channel angular extrusion (PTCAE) [44], equal channel angular pressing (ECAP) [42,45], ECAP with following HPT [42], ECAP with following cold rolling [46], simple shear extrusion (SSE) [47,48] and constrained groove pressing (CGP) [49].

For HPT, the steady-state grain size depends on strain rate, pressure, and temperature of processing [4,29]. It is important that the grain size in the dynamic equilibrium can be reached not only "from the top" but also "from the bottom". For example, if the coarse-grained steel is subjected to HPT, the grains are refined down to 15–20 nm [35,50–56]. On the other hand, if one takes the nanocrystalline steel with grain size of 10 nm and subjects it to deformation, the grains do not refine further, but grow up to the same steady-state value of 15–20 nm [20]. Similar behaviour was also observed for the grain size in nickel [57,58] and copper [59]. The Vickers microhardness saturates during HPT as well [18,25,36,60–72]. Usually it increases during SPD and correlates with tensile strength [21,31,32,62,65,73–75]. The main strengthening mechanism is the Hall-Petch hardening driven by the grain refinement [76]. Similar to grain size, if the initial hardness of an alloy is higher than the steady-state one, then softening instead of hardening takes place during SPD [77].

We can state that grain size and hardness of a material in a stationary or steady-state deformation during HPT treatment is *equifinal* [12]. In other words, it is a function of HPT conditions (like temperature, pressure, strain rate), but not of the initial state of the sample (i.e. its grain size and hardness). Moreover, there is a certain sustainability area for the stationary or steady-state. That means the initial grain size and/or hardness values can evolve to the stationary state during HPT only if they are not too much away from the stationary grain size and/or hardness.

4.2. Dissolution/precipitation and T_{eff} in HPT stationary state

For a long time SPD has been generally established as a treatment leading to the grain refinement [11,68] and to the formation of supersaturated solid solution as well as dissolution of precipitates. However, the grain size decreases only if the grains in a material before SPD were larger than that ones at deformation steady-state. The grains will grow during SPD if their size was initially smaller. The same is true also for the hardening/softening during SPD. From this point of view, the dissolution/precipitation behaves similarly. In the steady-state of deformation, a certain concentration c_{ss} of alloying element reaches in the solid solution at the given conditions of SPD. The c_{ss} depends on the dynamic equilibrium between dissolution and precipitation. If the initial concentration in a solid solution c_{init} is below c_{ss}, it increases during SPD and precipitates dissolve. Otherwise, if $c_{init} > c_{ss}$, the concentration of second component in a solid solution decreases and new precipitates appear (so-called dynamic ageing). For the first time it was found in Al–Zn alloys [78]. Now it is an established topic for investigations and the instrument for tailoring the properties of materials [79].

In previous works we observed the phenomenon of dissolution/precipitation for Cu–Ag [3], Cu–Sn [5] and Cu–Co [2] alloys only in a relatively narrow interval of c_{init} concentrations close to the c_{ss} value. The goal of this work was to study this phenomenon for the broad c_{init} range in order to determine experimentally, how wide is sustainability interval of c_{init} where c_{init} can evolve to c_{ss} during HPT. It was done both for Cu–Ag and for Cu–Sn alloys (see Figs. 1, 8 and 11). In the Cu–Ag system, the steady state lattice parameter is about 0.3634 nm. If the lattice parameter in (Cu) solid solution before HPT is below 0.3634 nm, the HPT leads to the increase of (Cu) lattice

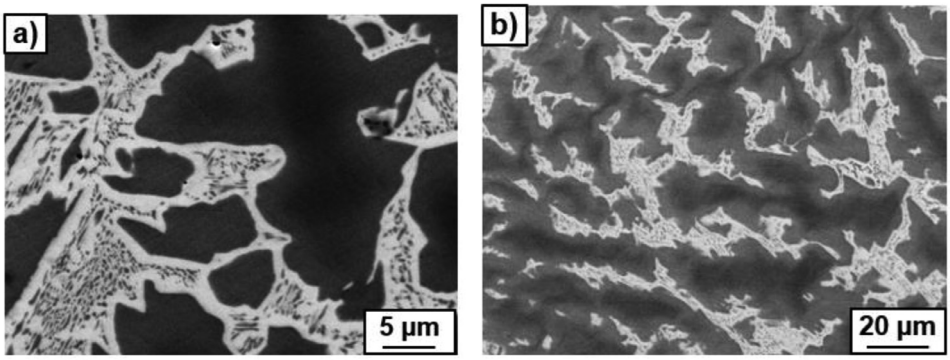

Fig. 9. SEM micrographs of Cu–14 wt. % Sn alloy annealed at 320 °C for 1200 h before (a) and after (b) HPT.

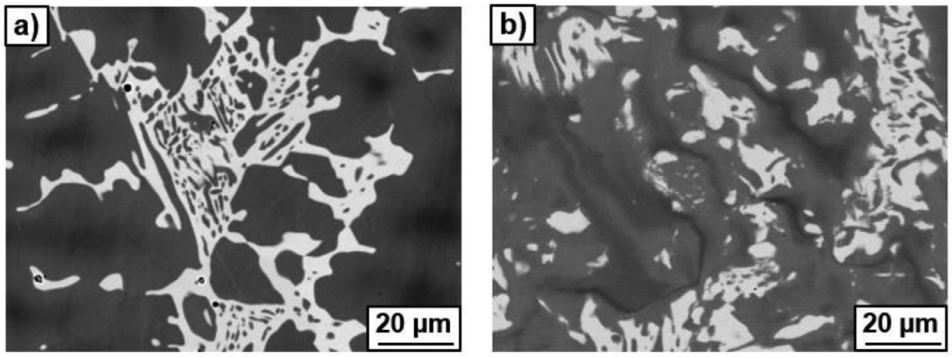

Fig. 10. SEM micrographs of Cu–14 wt. %Sn alloy annealed at 370 °C for 715 h before (a) and after (b) HPT.

parameter, i.e. to the increase of silver content in (Cu). If the lattice parameter in (Cu) solid solution before HPT is above 0.3634 nm, HPT leads to its decrease, i.e. to the decrease of silver content in (Cu). In all samples, the lattice parameter comes very close to the 0.3634 nm value after HPT, but it separates the states with either decomposition or enrichment of (Cu) solid solution. According to the Vegards law [3] the lattice parameter of 0.3634 nm corresponds to about c_{ss} = 5.5± 0.1 wt. % Ag dissolved in the (Cu) solid solution. The c_{ss} value is shown in the Cu–Ag phase diagram (Fig. 1a) by the vertical dashed line. The vertical dashed line intersects the solvus line (i.e. the line of maximum solubility of silver atoms in copper-based solid solution) at about 700±10 °C. We called earlier this value as "effective temperature", T_{eff} [3]. Georges Martin originally proposed this term to describe phase transformations driven by irradiation effects [80]. The idea of this term is to imply that the sample after severe treatment contains such phases as if it has been annealed at some elevated temperature T_{eff}. In our case the Cu–Ag samples after HPT contain the (Cu) solid solution with such concentration as if they were annealed at T_{eff} = 700±10 °C. In this work the value T_{eff} = 700±10 °C is determined basing on the analysis of twelve samples before and after HPT. Nevertheless, it is very close to the T_{eff} = 600±10 °C estimated in our first experiment with only two samples, one with $c_{init} < c_{ss}$ and one with $c_{init} > c_{ss}$ [3].

We can also consider the phenomenon of T_{eff} from the viewpoint of non-equilibrium thermodynamics [6–9]. The values of T_{eff} attributed to studied copper alloys reach hundreds of Kelvin degrees. However, the sample during HPT at T_{HPT} in ambient conditions becomes only a little bit warm. It is because at the stationary state during HPT the amount of lattice defects is so high that it cannot be described any more by the equilibrium *p-T-c* phase diagrams from handbook [10], which originates from the condition of free enthalpy minimum [6,7]. In the case of HPT, other dynamic phase diagrams should exist depending on the HPT parameters. These diagrams might be performed taking into account the condition of minimum entropy production [7]. The noted condition describes the equifinal stationary states in the linear non-equilibrium thermodynamics [7]. Such diagrams for HPT states are still unknown, as distinguished from equilibrium *p-T-c* phase diagrams involved in handbook [10]. However, it looks that the HPT processes are not very far from equilibrium and, therefore, the phases formed under HPT at T_{HPT} in ambient conditions still can be found in the handbook [10] but at higher T_{eff}.

In Cu–Sn system the steady state lattice parameter is about 0.3693 nm. If the lattice parameter in (Cu) solid solution before HPT is below 0.3693 nm, the HPT leads to the increase of (Cu) lattice parameter, i.e. to the increase of tin content in (Cu). If the lattice parameter in (Cu) solid solution before HPT is above 0.3693 nm, HPT leads to its decrease, i.e. to the decrease of tin content in (Cu). Differently to the Cu–Ag, not in all Cu–Sn samples the lattice parameter comes very close to the 0.3693 nm value after HPT (see Fig. 15). However, similar to Cu–Ag alloys, the 0.3693 nm value separates the states with either decomposition of (Cu) solid solution or its enrichment. According to the Vegards law [5] the lattice parameter of 0.3693 nm corresponds to about c_{ss} = 13.1±0.1 wt. % Sn dissolved in the (Cu) solid solution. This value c_{ss} is shown in the Cu–Sn phase diagram (Fig. 1b) by the vertical dashed line. At lower annealing temperatures, the tin concentration in (Cu) increases during HPT but remains below c_{ss}. In comparison with the Cu-Ag alloys subjected HPT, this fact can be explained by different nature of the secondary phases in Cu-Sn and Cu-Ag systems. Most probably, in the case of Cu–Ag alloys, the silver atoms migrate into solid solution from the interfaces between copper matrix and rather soft silver precipitates. The micrographs in Figs. 2 and 3 witness that HPT easily disintegrates and divides the large Ag particles. In the case of Cu–Sn alloys, the sources of tin atoms are the precipitates of quite hard ε and δ intermetallics. The micrographs in Figs. 9–11 show that, indeed, the large ε and δ particles remain almost unchanged and almost no HPT-driven fragmentation takes place. In Ref. [3] we analyzed the dissolution kinetics of silver atoms from Ag precipitates. It was controlled by the

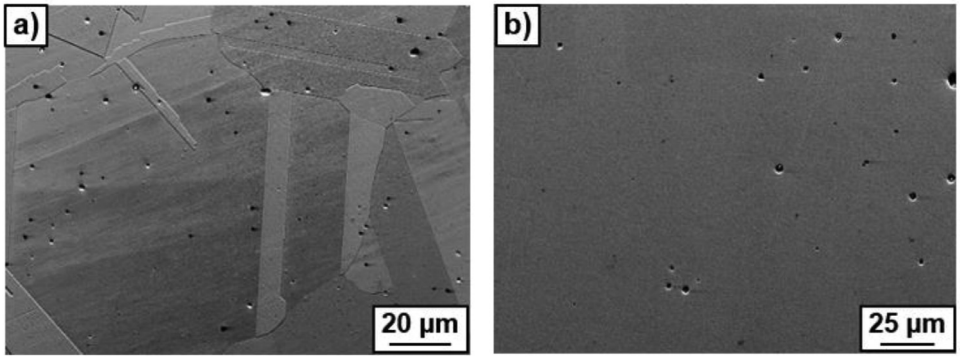

Fig. 11. SEM micrographs of Cu–14 wt. %Sn alloy annealed at 500 °C for 894 h before (a) and after (b) HPT.

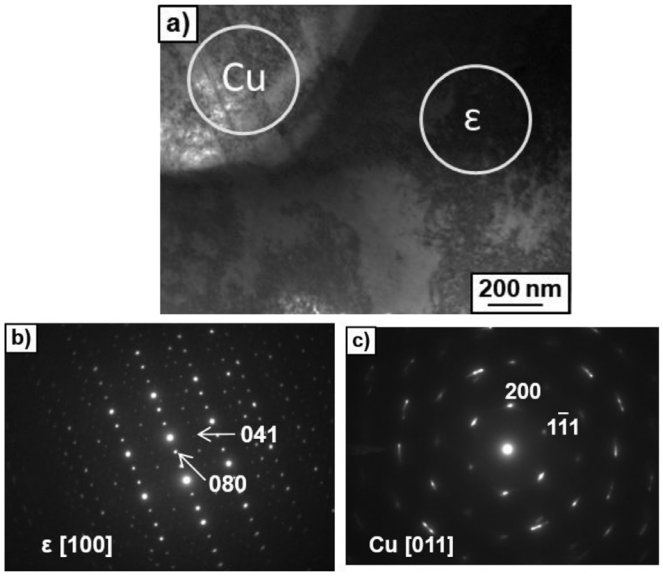

Fig. 12. Bright field (a) TEM micrograph and selected area electron diffraction patterns (b, c) of Cu–14 wt. % Sn alloy after HPT deformation, previously annealed at 320 °C for 1200 h. The rings in (a) show the areas where the SAED have been taken.

specific area of Cu/Ag interphase boundaries. In the case of soft and small Ag precipitates, the specific area of such interphase boundaries is high enough. In the case of hard ε and δ Cu–Sn intermetallic particles, they cannot ensure sufficient amount of tin atoms during HPT. Thus, the lower initial concentrations c_{init} in (Cu) matrix tend during

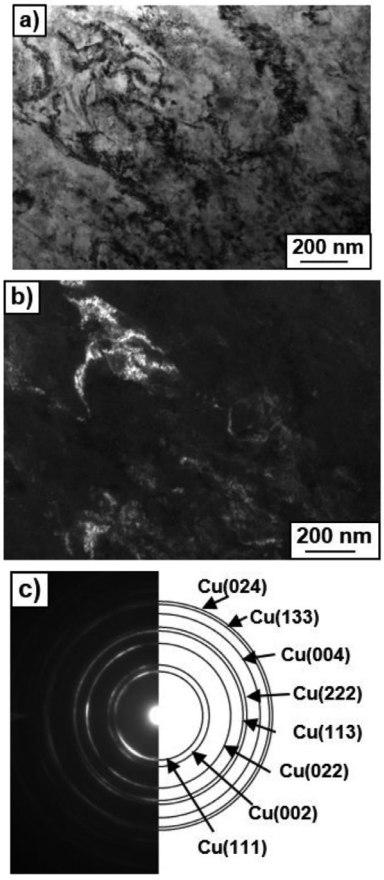

Fig. 13. Bright field (a) and dark field (b) TEM micrographs with selected area electron diffraction pattern (c) of Cu –14 wt. % Sn alloy after HPT deformation, previously annealed at 500 °C for 894 h.

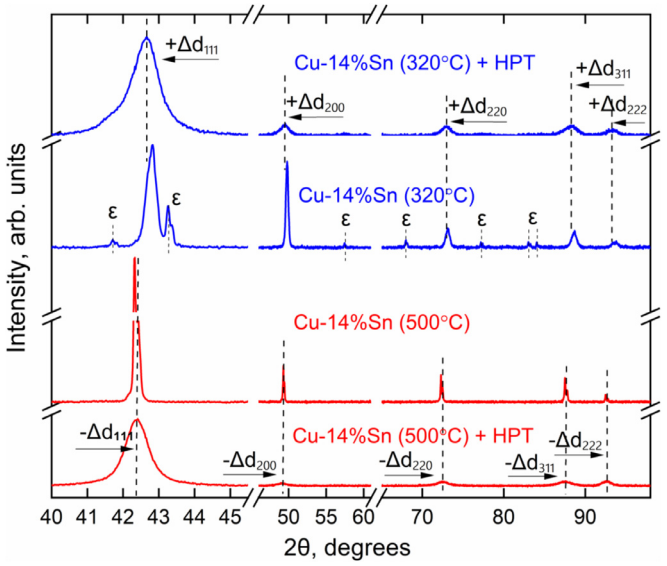

Fig. 14. X-ray diffraction pattern of Cu-14 wt. % Sn alloy before and after HPT deformation previously annealed at 320 and 500 °C.

HPT although towards higher concentration but still remain below than c_{ss} value (Fig. 1b).

In Fig. 1b the vertical dashed line at c_{ss} = 13.1±0.1 wt. % Sn intersects the solvus line (i.e. the line of maximum solubility of tin atoms in copper-based solid solution) at about T_{eff} = 400±10 °C. In our case the Cu–Sn samples after HPT contain the (Cu) solid solution with such concentration as if they were annealed at T_{eff} = 400±10 °C. In this work the value T_{eff} = 400 °C±10 °C is determined basing on the analysis of nine samples before and after HPT. Nevertheless, it is very close to the T_{eff} = 420 °C estimated in our first experiment with only two samples, one with $c_{init} < c_{ss}$ and another one with $c_{init} > c_{ss}$ [5].

So, we observed that the sustainability area between any of inintial c_{init} and estimated c_{ss} values for the HPT stationary state is surprisingly wide for the dissolution/precipitation competition. In case of Cu–Ag alloys (Figs. 1 and 8) c_{init} can be as low as 0.1c_{ss}, and nevertheless the composition of solid solution reaches c_{ss} after HPT. It means c_{ss} = 5.5±0.1 wt. % Ag is the unique attractor for the HPT

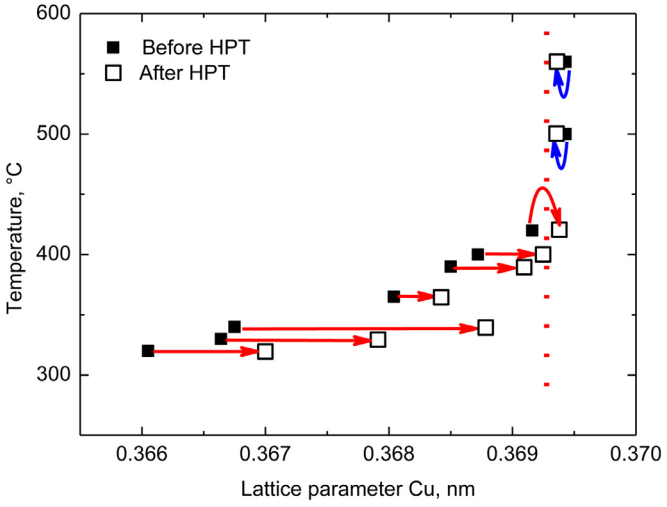

Fig. 15. Dependence of lattice parameter in the (Cu) matrix solid solution of Cu–Sn alloys on annealing temperature before and after HPT. The solid squares show the concentration in (Cu) after annealing before HPT. The open squares are for the concentration in the (Cu) matrix solid solution after annealing and HPT. Red arrows indicate how the concentration in (Cu) changes after HPT. Vertical dotted line shows the concentration c_{ss}.

dissolution/precipitation for Cu–Ag alloys between 0 and 8.5 wt. %Ag (Fig. 1). In case of Cu–Sn alloys (Figs. 1 and 15) we also observe the equifinality and unique attractor at c_{ss} = 13.1±0.1 wt. % Sn for the HPT dissolution/precipitation. However, the situation in Cu–Sn alloys is more complicated due to the hard intermetallic precipitates.

We have to underline here that the evolution of initial structure towards the steady-state one is strongly dependent on the initial morphology (particle size) of the phases. Moreover, the steady state itself depends on the exact strain and strain mode. In this work we excluded the second factor by using the same SPD mode (HPT) under constant and equal conditions (construction of the anvils, same pressure, same rotation speed, same revolutions number). We discussed above the influence of SPD mode on the microstructure of SPD-treated copper alloys (see Section 4.1). The important indication of the initial structure influence on the evolution towards the steady-state is the fact that the points for Cu–Sn alloys at low annealing temperatures (differently to the Cu–Ag alloys) move towards c_{ss}, but do not reach it (see Figs. 1, 8 and 15). This can be caused by the fact that silver particles in Cu–Ag alloys are rather soft, but ε and δ intermetallics in Cu–Sn alloys are quite hard. As it was shown recently for steel and Cu/CuZr nanolaminates, the properties of second phase strongly influence the process of shear-induced mixing and control the co-deformation of crystalline-amorphous nanolaminates and steels [81–83]. Different initials states can also modify the evolution of mechanical properties in the transient state and even change the time needed to reach the dynamic equilibrium itself [84].

Important to note as well that the dynamic equilibrium between production and relaxation of defects is a very general phenomenon. For example, it can also lead to the dynamic equilibrium between amophization of crystalline phases and formation of crystals in the amorphous phase under HPT [85]. It is possible also to estimate then the value of T_{eff} by finding the respective phase field in the equilibrium phase diagram [18,19]. Following the idea of Georges Martin, the amorphous phase in the sample during HPT would be equivalent to the liquid phase in the equilibrium phase diagram [80].

4.3. Kinetic properties and grain boundaries in the HPT stationary state

In Section 4.2 we determined the sustainability areas between c_{init} and c_{ss} for the HPT stationary state during the dissolution/precipitation competition in Cu–Ag and Cu–Sn alloys. The stationary solubility c_{ss} under HPT at ambient conditions corresponds to the equilibrium solubility in copper-based solid solution at certain elevated T_{eff}. It is because the non-equilibrium phase diagrams for open systems differs from equilibrium ones. One can expect that not only dissolution/precipitation competition under HPT leads to solubility, which differs from that at, for example, room temperature and is equivalent to that at T_{eff}. Indeed, we can find another processes or properties characterizing the sample state or structure as not corresponding to the equilibrium one at room temperature, but to that at some elevated T_{eff}. Below we discuss four other phenomena permitting to estimate T_{eff} for HPT treatment, namely the deformation of intermetallic compounds, accelerated mass transfer, grain boundary (GB) faceting and GB segregation.

4.3.1. HPT of intermetallic compounds

The existence of dynamic equilibrium between the precipitation and dissolution of precipitates was used for T_{eff} estimation. However, not only the equilibrium composition of solid solution could be taken in consideration. Previously we studied the HPT-driven phase transformations between Hume-Rothery phases in Cu–Sn alloys [86]. In the initial state before HPT the sample contained the mixture of ζ+ε phases. After HPT sample consists of the δ+ε phases as after the long annealing between 350 and 400 °C [86]. Thus, the value T_{eff} = 400± 10 °C determined in this work basing on the precipitation/dissolution transition correlates well with the noted previous result obtained for HPT of intermetallics.

4.3.2. Accelerated mass transfer

The HPT-driven dissolution and precipitation in Cu-based alloys proceed quite quickly. The model developed in [3] for the HPT-driven mass transfer (supposed to be controlled by the bulk diffusion) gives the value for bulk diffusion coefficient D_{HPT} = 3•10^{-16} m^{2}s^{-1}. The extrapolation of the literature values towards the HPT temperature T_{HPT} = 25 °C gives D = 10^{-35} m^2/s for self-diffusion in Cu [87] and D = 10^{-38} m^2/s for tracer diffusion of Ag in Cu [88]. So, the HPT-driven mass transfer is about 19 orders of magnitude faster than conventional bulk diffusion at T_{HPT}. It occurs in spite of the fact that the applied pressure of 6 GPa additionally slows down the diffusion as well as GB migration [89–91]. Therefore, we have to consider the deformation-driven mechanisms of mass transfer. On the other hand, the value D = 3•10^{-16} m^{2}s^{-1} is close to the bulk self-diffusivity in pure copper at ~650 °C [87] and to the bulk tracer diffusion of Ag in Cu at ~600 °C [88]. These values are comparable to T_{eff} = 700±10 °C obtained from the c_{ss} measurement in this work (Figs. 1 and 8).

One can also use the simple model for the estimation of D controlling mass-transfer in HPT experiments [92]. The small Co particles were partly dissolved during t = 300 s of HPT treatment. The diffusion path in this case would be equal to the distance between fine Co precipitates in the initial sample, i.e. d = 200 nm. It corresponds to the bulk diffusion coefficient of $D_{HPT} = (d\ t)^{-2}$ = 10^{-16} m^{2}s^{-1}. This is very close to the above estimation for the Cu–Ag alloys [3]. The extrapolation of the literature values towards the T_{HPT} gives D = 10^{-38} m^2/s for diffusion of Co in Cu [93]. This value is also about 19 orders of magnitude lower than estimated D_{HPT}. Again, D_{HPT} is equal to the bulk diffusion of Co in Cu at ~600 °C [93]. This value is somewhat lower than T_{eff} = 900±20 °C for HPT in Cu–Co alloys [94].

Similar estimation has been made for Cu–Sn alloys [5]. The HPT-driven mass-transfer can be considered as controlled by bulk diffusion with coefficient of $D_{HPT} = (d\ t)^{-2}$ = 10^{-16} m^{2}s^{-1}. The extrapolation of the literature values to T_{HPT} gives D = 10^{-31} m^2/s for diffusion of Sn in Cu [94]. It is about 15 orders of magnitude lower than estimated D_{HPT}. Thus, D_{HPT} is equal to the bulk diffusion of Sn in Cu at ~600 °C [94] which is somewhat higher than T_{eff} = 400±10 °C obtained from the c_{ss} measurement in this work (Figs. 1 and 8). We can conclude that the estimated bulk diffusion coefficients for the HPT-driven mass-transfer are much closer to the respective diffusion coefficients for self diffusion in copper and tracer diffusion of Co, Ag and Sn at T_{eff} than at HPT temperature T_{HPT}.

In addition to the bulk phase transformations discussed above, one can investigate the influence of HPT on the structure of grain boundaries (GBs) and GB phase transitions assuming, in particular, GB segregation and GB faceting/roughening.

4.3.3. GB segregation

In the binary, ternary and multicomponent systems a part of diluted atoms segregate in GBs. In other words, the concentration of diluted atoms in GBs c_{GB} differs from that in the bulk of matrix grains, c_b. Their ratio $s = c_{GB}/c_b$ is called GB segregation factor. Most frequently $s > 1$. In copper-based alloys s and segregation enthalpy H_s has been measured by radiotracer method, Auger electron spectroscopy (AES) and atom probe tomography (APT) [95–111]. The HPT leads to the strong grain refinement. In Cu-based alloys the grain size typically decreases from several hundreds of microns to 100-200 nm [4,112,113]. As a result, a lot of new GBs are formed during HPT together with those segregation layers. In order to construct those GB novel segregation layers, one needs the solute atoms. If the total solute concentration in the sample $c_{tot} > c_{ss}$, the sample contains the particles of a second phase and they originate as a source of solute atoms for the segregation layers in the newly formed GBs. On the contrary, if $c_{tot} < c_{ss}$, the sample contains only the solid solution. In

this case, the solid solution originates as a source of solute atoms for the segregation layers in the newly formed GBs. As a result, the concentration of a second component in the matrix decreases, and in the case of strong GB segregation this decrease is measurable by shift of Cu peaks in XRD patterns, i.e. changes in lattice parameter [95]. In such a way, we observed the GB segregation in Cu–Co, Cu–Ag and Cu–In alloys after HPT [95]. The measured values of s were found to be 71 for cobalt in copper GBs, 10 for silver atoms and only about 1 for indium atoms. The data for s and H_s measured for the Cu–Co and Cu–Ag alloys by radiotracer method and AES [78–90] permit to extrapolate s values to the temperature of HPT treatment of about 25 °C. Such extrapolation gives $s > 10^3–10^4$ [95]. The values of s = 71 for the Cu–Co and s = 10 for Cu–Ag alloys after HPT correlate with the radiotracer data of s at high temperature of $T >$ 500 °C. In other words, the GB enrichment after HPT is equivalent to that in the samples annealed at a certain elevated temperature, which can be called as GB segregation effective temperature $T_{effSegr} >$ 500 °C.

4.3.4. GB faceting/roughening

Similar to the free surfaces of single crystals (like very well-known salt, sugar, diamond etc.), GBs can also possess the flat segments called facets [114]. The facets of free surfaces are parallel to the most highly dense packed atomic planes in the crystal lattice. In the case of GBs, the so-called coincidence site lattice (CSL) [115] plays the role similar to that of crystal lattice for surface facets. The GB facets are observed mainly in the GBs with CSLs with high density of coincidence sites and, therefore, low Σ value (so-called coincidence GBs) [116]. The coincidence GBs usually exhibit low energy, migration rate, diffusion permeability, and high strength [117,118]. With increasing temperature, the flat facets can lose their stability as a result of so-called faceting-roughening transition at a certain temperature T_R [119–121]. The temperature of faceting-roughening transition depends on the "perfection" of free surface or GB [122]. T_R is higher for free surfaces or GBs densely packed by the lattice or CSL nodes [123–125]. In Ref. [126] we experimentally constructed the phase diagram for the facets of Σ3 twin and Σ9 GBs in high-purity 5N5 copper. At high temperatures only symmetric twin facets $(111)_1//(111)_2$ exist corresponding to the most densely packed Σ3 CSL plane $(100)_{\Sigma 3CSL}$ together with non-CSL 9*R* facets [126]. With decreasing temperature the new and new facets consequently appear with less densely packed Σ3 CSL planes like $(010)_{\Sigma 3CSL}$, $(110)_{\Sigma 3CSL}$, $(110)_{\Sigma 3CSL}$, $(130)_{\Sigma 3CSL}$. On the other hand, we observed that by HPT of a very pure copper (same 5N5 copper like in [126]), the dynamic recrystallization takes place deep in the HPT sample [127,128]. Thus, the recrystallization twins are clearly visible in the HPT samples, and the spectrum of crystallographically different facets can be analyzed [129]. As a result, the structure of facets in the Σ3 twin GBs after HPT corresponds to the state at T_{effFac} = 620±50 °C [129]. In other words, the GB faceting after HPT is equivalent to that in the samples annealed at a certain elevated temperature which can be called as GB faceting effective temperature T_{effFac} = 620±50 °C.

4.3.5. General remarks

The performed investigation established that the sustainability area (i.e. interval for the c_{init} concentrations) for the HPT-driven competition between dissolution and precipitation is quite broad for Cu–Ag and Cu–Sn alloys. In other words, the steady state concentration c_{ss} is equifinal and "attracts" the composition of solid solution from very wide interval of initial concentrations, c_{init}, both higher and lower than c_{ss}. Moreover, the stationary solubility c_{ss} during HPT at T_{HPT} corresponds to the equilibrium solubility in copper-based solid solution at certain elevated T_{eff}. It is because the non-equilibrium phase diagrams for open systems differ from equilibrium ones.

We observed that not only the HPT-driven precipitation/dissolution competition permits to estimate the value of the (elevated) effective temperature T_{eff}. Four other HPT-driven processes like transformations between intermetallics, accelerated mass transfer, grain boundary faceting and grain boundary segregation also witness that the state of material during SPD (i.e. in non-equilibrium stationary conditions) at T_{HPT} is equivalent to that in an equilibrium system but at elevated temperature T_{eff}. The most reliable explanation of these facts is based on the idea that in the steady state during HPT the rate of the defects production by the external force is equal to the rate of defects annihilation. As a result, the steady-state concentration of defects (like vacancies, dislocations, GBs etc) is higher than in the equilibrium at the HPT temperature T_{HPT} (usually close to RT). The high vacancy concentration during HPT has been directly observed recently using the in situ synchrotron irradiation [130–132]. As it is well known, the increase of temperature leads to the increase of equilibrium vacancy concentration. Thus, one can consider the increased vacancy concentration during HPT (i.e. in non-equilibrium stationary conditions) as an equivalent of increased temperature in an equilibrium system. This fact explains why the observed T_{eff} is always higher than T_{HPT} in Cu-based alloys.

However, why T_{eff} is so different for Cu–Ag and Cu–Sn alloys? It is because in the steady state during HPT the rate of the defects production induced by the external force is equal to the rate of defects annihilation. In both cases, the external mechanical influence is the same (geometry of HPT machine, deformation rate, pressure and temperature, and even the hardness of Cu-matrix). However, the rate of defects annihilation is different. It is because during the diffusion-like mass transfer the potential barrier has to be overcome for each atom jumping into the neighboring lattice node. The height of this barrier is lower for tin atoms in copper matrix than for the silver ones. Moreover, we observed the linear correlation between T_{eff} for different alloying elements in copper and their enthalpy of bulk diffusion H_d [4]. T_{eff} increases nearly linear with increasing H_d. In other words, lower H_d facilitates the annihilation of defects, the steady-state vacancy concentration decreases, it is equivalent to the decrease of temperature, and, as a result, T_{eff} becomes lower as well.

Thus, the observed correlation between T_{eff} and H_d permits to predict the behavior of copper-based alloys during HPT. For a certain alloying element one can find the H_d value in the handbook, then estimate the T_{eff} value from the graph [4]. In turn, the T_{eff} permits to estimate the c_{ss} from the respective phase diagram (see Fig. 1). By knowing the c_{ss} one can predict the precipitation/dissolution processes in the alloys and tailor the materials' behavior during SPD.

5. Conclusions

The HPT of binary Cu–Ag and Cu–Sn alloys has been studied. The preliminary annealing before HPT produces the samples with broad spectrum of initial concentration c_{init} of silver and tin in the matrix solid solution. During HPT, a certain steady-state concentration c_{ss} of the alloying element is reached in the matrix. The measured c_{ss} values were 5.5±0.1 wt. % Ag and 13.1±0.1 wt. % Sn. If the initial concentration c_{init} in Cu matrix was below c_{ss} ($c_{init} < c_{ss}$), it increased towards c_{ss} during HPT. If $c_{init} > c_{ss}$ it decreased towards c_{ss}. We observed that c_{ss} did not depend on c_{init} in broad interval of c_{init} and was, therefore, equifinal. We explained this phenomenon by the competition between decomposition of a solid solution with dissolution of precipitates during HPT. The established dynamic equilibrium between precipitation and dissolution led to a certain c_{ss} of the alloying element in the matrix. In Cu-based alloys, the obtained T_{eff} is always higher than T_{HPT} and correlates with activation enthalpy of dopant diffusion in Cu. Other HPT-driven phenomena such as accelerated mass transfer, intermetallic phase formation, grain boundary faceting and grain boundary segregation were taken into account to evaluate the effective temperature T_{eff}.

Declaration of Competing Interest

The authors declare that they have no known competing financial interests or personal relationships that could have appeared to influence the work reported in this paper.

Acknowledgements

This research was partially funded by the National Science Centre of Poland (grant OPUS, 2014/13/B/ST8/04247), by the Russian Foundation for Basic Research (grants 18-38-20145 and 18-03-00067), state task of ISSP and CSC RAS as well as Karlsruhe Nano Micro Facility (KNMF), a Helmholtz Research Infrastructure at Karlsruhe Institute of Technology (KIT).

References

[1] B.B. Straumal, B. Baretzky, A.A. Mazilkin, F. Phillipp, O.A. Kogtenkova, M.N. Volkov, R.Z. Valiev, Formation of nanograined structure and decomposition of supersaturated solid solution during high pressure torsion of Al-Zn and Al-Mg, Acta Mater. 52 (2004) 4469–4478.
[2] B. Straumal, A.R. Kilmametov, Yu.O. Kucheev, L. Kurmanaeva, Yu. Ivanisenko, B. Baretzky, A. Korneva, P. Zięba, D.A. Molodov, Phase transitions during high pressure torsion of Cu-Co alloys, Mater. Lett. 118 (2014) 111–114.
[3] B.B. Straumal, V. Pontikis, A.R. Kilmametov, A.A. Mazilkin, S.V. Dobatkin, B. Baretzky, Competition between precipitation and dissolution in Cu-Ag alloys under high pressure torsion, Acta Mater. 122 (2017) 60–71.
[4] B.B. Straumal, A.R. Kilmametov, A. Korneva, A.A. Mazilkin, P.B. Straumal, P. Zięba, B. Baretzky, Phase transitions in Cu-based alloys under high pressure torsion, J. Alloy. Compd. 707 (2017) 20–26.
[5] B.B. Straumal, A.R. Kilmametov, I.A. Mazilkin, A. Korneva, P. Zięba, B. Baretzky, Phase transformations in copper-tin solid solutions at high-pressure torsion, JETP Lett. 110 (2019) 624–628.
[6] I. Prigogine, Introduction to Thermodynamics of Irreversible Processes, J. Wiley & Sons, New York, London, 1955.
[7] G. Nikolis, I. Prigogine, Self-Organization in Non-equilibrium Systems, J. Wiley & Sons Inc., New York, London, 1977.
[8] D. Kondepudi, I. Prigogine, Modern Thermodynamics. From Heat Engine to Dissipative Structures, second ed., J. Wiley & Sons Ltd., Chichester, UK, 2015.
[9] I. Prigogine, I. Stengers, Order Out of Chaos, Man's New Dialog with Nature, Verso, London, New York, 2017.
[10] T.B. Massalski (Ed.), Binary Alloy Phase Diagrams, second ed.ASM International, Materials Park, OH, 1990.
[11] R.Z. Valiev, R.K. Islamgaliev, I.V. Alexandrov, Bulk nanostructured materials from severe plastic deformation, Prog. Mater. Sci. 45 (2000) 103–189.
[12] L. von Bertalanffy, The theory of open systems in physics and biology, Science 111 (1950) 23–29.
[13] B.B. Straumal, A.R. Kilmametov, Yu. Ivanisenko, A.A. Mazilkin, O.A. Kogtenkova, L. Kurmanaeva, A. Korneva, P. Zięba, B. Baretzky, Phase transitions induced by severe plastic deformation: steady-state and equifinality, Int. J. Mater. Res. 106 (2015) 657–664.
[14] R.Z. Valiev, Yu.V. Ivanisenko, E.F. Rauch, B. Baudelet, Structure and deformation behaviour of armco iron subjected to severe plastic deformation, Acta Metall. 44 (1996) 4705–4712.
[15] A.V. Korznikov, G. Tram, O. Dimitrov, G.F. Korznikova, S.R. Idrisova, Z. Pakiela, The mechanism of nanocrystalline structure formation in Ni_3Al during severe plastic deformation, Acta Mater. 49 (2001) 663–671.
[16] M. Wojdyr, Fityk: a general-purpose peak fitting program, J. Appl. Cryst. 43 (2010) 1126–1128.
[17] P. Zięba, Recent developments on discontinuous precipitation, Arch. Metal. Mater. 62 (2017) 955–968.
[18] B.B. Straumal, A.R. Kilmametov, A.A. Mazilkin, S.G. Protasova, K.I. Kolesnikova, P.B. Straumal, B. Baretzky, Amorphization of Nd-Fe-B alloy under the action of high-pressure torsion, Mater. Lett. 145 (2015) 63–66.
[19] B.B. Straumal, A.A. Mazilkin, S.G. Protasova, D.V. Gunderov, G.A. López, B. Baretzky, Amorphization of crystalline phases in the Nd-Fe-B alloy driven by the high-pressure torsion, Mater. Lett. 161 (2015) 735–739.
[20] C. Borchers, C. Garve, M. Tiegel, M. Deutges, A. Herz, K. Edalati, R. Pippan, Z. Horita, R. Kirchheim, Nanocrystalline steel obtained by mechanical alloying of iron and graphite subsequently compacted by high-pressure torsion, Acta Mater: 97 (2015) 207–215.
[21] S. Lee, Z. Horita, High-pressure torsion for pure chromium and niobium, Mater. Trans. 53 (2012) 38–45.
[22] K. Edalati, S. Toh, M. Watanabe, Z. Horita, In situ production of bulk intermetallic-based nanocomposites and nanostructured intermetallics by high-pressure torsion, Scr. Mater. 66 (2012) 386–389.
[23] J.M. Cubero-Sesin, Z. Horita, Strengthening via microstructure refinement in bulk Al4 mass% fe alloy using high-pressure torsion, Mater. Trans. 53 (2012) 46–55.
[24] K. Bryła, J. Morgiel, M. Faryna, K. Edalati, Z. Horita, Effect of high-pressure torsion on grain refinement, strength enhancement and uniform ductility of EZ magnesium alloy, Mater. Lett. 212 (2018) 323–326.
[25] A.A. Mazilkin, B.B. Straumal, S.G. Protasova, O.A. Kogtenkova, R.Z. Valiev, Structural changes in Al alloys upon the severe plastic deformation, Phys. Solid State 49 (2007) 868–873.
[26] B.B. Straumal, O.A. Kogtenkova, S.G. Protasova, P. Zięba, T. Czeppe, B. Baretzky, R.Z. Valiev, First measurement of the heat effect of the grain boundary wetting phase transition, J. Mater. Sci. 46 (2011) 4243–4247.
[27] K. Edalati, D.J. Lee, T. Nagaoka, M. Arita, H.S. Kim, Z. Horita, R. Pippan, Real hydrostatic pressure in high-pressure torsion measured by bismuth phase transformations and FEM simulations, Mater. Trans. 57 (2016) 533–538.
[28] K. Edalati, Y. Hashiguchi, P.H.R. Pereirac, Z. Horita, T.G. Langdon, Effect of temperature rise on microstructural evolution during high-pressure torsion, Mater. Sci. Eng. A 714 (2018) 167–171.
[29] K. Edalati, Z. Horita, High-pressure torsion of pure metals: Influence of atomic bond parameters and stacking fault energy on grain size and correlation with hardness, Acta Mater 59 (2011) 6831–6836.
[30] K. Edalati, Z. Horita, T. Furuta, S. Kuramoto, Dynamic recrystallization and recovery during high-pressure torsion: Experimental evidence by torque measurement using ring specimens, Mater. Sci. Eng. A 559 (2013) 506–509.
[31] A.A. Mazilkin, O.A. Kogtenkova, B.B. Straumal, R.Z. Valiev, B. Baretzky, Formation of nanostructure during high-pressure torsion of Al-Zn, Al-Mg and Al-Zn-Mg alloys, Def. Diff. Forum 237–240 (2005) 739–744.
[32] A.A. Mazilkin, B. Baretzky, S. Enders, O.A. Kogtenkova, B.B. Straumal, E.I. Rabkin, R.Z. Valiev, Hardness of nanostructured Al-Zn, Al-Mg and Al-Zn-Mg alloys obtained by high-pressure torsion, Def. Diff. Forum 249 (2006) 155–160.
[33] R. Kulagin, Y. Beygelzimer, Yu. Ivanisenko, A. Mazilkin, B. Straumal, H. Hahn, Instabilities of interfaces between dissimilar metals induced by high pressure torsion, Mater. Lett. 222 (2018) 172–175.
[34] K. Bryła, M. Krystian, J. Horky, B. Mingler, K. Mroczka, P. Kurtyka, L. Lityńska-Dobrzyńska, Improvement of strength and ductility of an EZ magnesium alloy by applying two different ECAP concepts to processable initial states, Mater. Sci. Eng. A 737 (2018) 318–327.
[35] E.A. Lukyanova, N.S. Martynenko, V.N. Serebryany, A.N. Belyakov, L.L. Rokhlin, S.V. Dobatkin, Y.Z. Estrin, Structure and mechanical and corrosion properties of a magnesium Mg–Y–Nd–Zr alloy after high pressure torsion, Russ. Metall. 11 (2017) 912–921.
[36] P. Krala, J. Dvorak, V. Sklenicka, T. Masuda, Z. Horita, K. Kucharova, M. Kvapilova, M. Svobodova, Microstructure and creep behaviour of P92 steel after HPT, Mater. Sci. Eng. A 723 (2018) 287–295.
[37] S. Sabbaghianrad, S.A. Torbati-Sarraf, T.G. Langdon, An investigation of the limits of grain refinement after processing by a combination of severe plastic deformation techniques: a comparison of Al and Mg alloys, Mater. Sci. Eng. A 712 (2018) 373–379.
[38] K. Tirsatine, H. Azzeddine, Y. Huang, T. Baudin, A.-L. Helbert, F. Brisset, D. Bradai, T.G. Langdon, An EBSD analysis of Fe-36%Ni alloy processed by HPT at ambient and a warm temperature, J. Alloy. Compd. 753 (2018) 46–53.
[39] M.Y. Alawadhi, S. Sabbaghianrad, Y. Huanga, T.G. Langdon, Direct influence of recovery behaviour on mechanical properties in oxygen-free copper processed using different SPD techniques: HPT and ECAP, J. Mater. Res. Technol. 6 (2017) 369–377.
[40] M. Azabou, T. Makhlouf, J. Saurin, L. Escoda, J.J. Suñol, M. Khitouni, A study of densification and phase transformations of nanocomposite Cu–Fe prepared by mechanical alloying and consolidation process, Int. J. Adv. Manuf. Technol. 87 (2016) 981–987.
[41] B.B. Straumal, A.A. Mazilkin, B. Baretzky, E. Rabkin, R.Z. Valiev, Accelerated diffusion and phase transformations in Co-Cu alloys driven by the severe plastic deformation, Mater. Trans. 53 (2012) 63–71.
[42] N. Lugo, N. Llorca, J.M. Cabrera, Z. Horita, Microstructures and mechanical properties of pure copper deformed severely by equal-channel angular pressing and high pressure torsion, Mater. Sci. Eng. A 477 (2008) 366–371.
[43] J. Čížek, M. Janeček, O. Srba, R. Kužel, Z. Barnovská, I. Procházka, S. Dobatkin, Evolution of defects in copper deformed by high-pressure torsion, Acta Mater 59 (2011) 2322–2329.
[44] M. Shamsborhan, M. Ebrahimi, Production of nanostructure copper by planar twist channel angular extrusion process, J. Alloy. Compd. 682 (2016) 552–556.
[45] C.L. Tang, H. Li, S.Y. Li, Effect of processing route on grain refinement in pure copper processed by equal channel angular extrusion, Trans. Nonferrous Met. Soc. China 26 (2016) 1736–1744.
[46] Z.N. Mao, R.C. Gu, F. Liu, Y. Liu, X.Z. Liao, J.T. Wang, Effect of equal channel angular pressing on the thermal-annealing-induced microstructure and texture evolution of cold-rolled copper, Mater. Sci. Eng. A 674 (2016) 186–192.
[47] E. Bagherpour, F. Qods, R. Ebrahimi, H. Miyamoto, Microstructure quantification of ultrafine grained pure copper fabricated by simple shear extrusion (SSE) technique, Mater. Sci. Eng. A 674 (2016) 221–231.
[48] E. Bagherpour, F. Qods, R. Ebrahimi, H. Miyamoto, Microstructure evolution of pure copper during a single pass of simple shear extrusion (SSE): role of shear reversal, Mater. Sci. Eng. A 666 (2016) 324–338.
[49] P.C. Yadav, A. Sinhal, S. Sahu, A. Roy, S. Shekhar, Microstructural inhomogeneity in constrained groove pressed Cu-Zn alloy sheet, J. Mater. Eng. Perform. 25 (2016) 2604–2614.
[50] A.V. Korznikov, Y.V. Ivanisenko, D.V. Laptionok, I.M. Safarov, V.P. Pilyugin, R.Z. Valiev, Influence of severe plastic deformation on structure and phase composition of carbon steel, Nanostruct. Mater. 4 (1994) 159–167.
[51] Y. Ivanisenko, W. Lojkowski, R.Z. Valiev, H.-J. Fecht, The mechanism of formation of nanostructure and dissolution of cementite in a pearlitic steel during high pressure torsion, Acta Mater. 51 (2003) 5555–5570.
[52] Y. Ivanisenko, R.K. Wunderlich, R.Z. Valiev, H.-J. Fecht, Annealing behaviour of nanostructured carbon steel produced by severe plastic deformation, Scr. Mater. 49 (2003) 947–952.
[53] J. Zrnik, R. Pippan, S. Scheriau, L. Kraus, M. Fujda, Microstructure and mechanical properties of UFG medium carbon steel processed by HPT at increased temperature, J. Mater. Sci. 45 (2010) 4822–4826.

[54] S. Bayramoglu, C.H. Gür, I.V. Alexandrov, M.M. Abramova, Characterization of ultra-fine grained steel samples produced by high pressure torsion via magnetic Barkhausen noise analysis, Mater. Sci. Eng. A 527 (2010) 927–933.
[55] J. Ning, E. Courtois-Manara, L. Kurmanaeva, A.V. Ganeev, R.Z. Valiev, C. Kübel, Y. Ivanisenko, Tensile properties and work hardening behaviors of ultrafine grained carbon steel and pure iron processed by warm high pressure torsion, Mater. Sci. Eng. A 581 (2013) 8–15.
[56] Y. Todaka, Y. Miki, M. Umemoto, C. Wang, K. Tsuchiya, Tensile property of submicrocrystalline pure Fe produced by HPT-straining, Mater. Sci. Forum 584–586 (2008) 597–604.
[57] X.Z. Liao, A.R. Kilmametov, R.Z. Valiev, H. Gao, X. Li, A.K. Mukherjee, J.F. Bingert, Y.T. Zhu, High-pressure torsion-induced grain growth in electrodeposited nanocrystalline Ni, Appl. Phys. Lett. 88 (2006) 021909.
[58] R. Pippan, S. Scheriau, A. Taylor, M. Hafok, A. Hohenwarter, A. Bachmaier, Saturation of fragmentation during severe plastic deformation, Annu. Rev. Mater. Res. 40 (2010) 319–343.
[59] H. Wen, R.K. Islamgaliev, K.M. Nesterov, R.Z. Valiev, E.J. Lavernia, Dynamic balance between grain refinement and grain growth during high-pressure torsion of Cu powders, Philos. Mag. Lett. 93 (2013) 481–489.
[60] K. Edalati, D. Akama, A. Nishio, S. Lee, Y. Yonenaga, J.M. Cubero-Sesin, Z. Horita, Influence of dislocation-solute atom interactions and stacking fault energy on grain size of single-phase alloys after severe plastic deformation using high-pressure torsion, Acta Mater. 69 (2014) 68–77.
[61] R. Tejedora, K. Edalati, J.A. Benito, Z. Horita, J.M. Cabrera, High-pressure torsion of iron with various purity levels and validation of Hall-Petch strengthening mechanism, Mater. Sci. Eng. A 743 (2019) 597–605.
[62] I.F. Mohamed, T. Masuda, S. Lee, K. Edalati, Z. Horita, S. Hirosawa, K. Matsuda, D. Terada, M.Z. Omar, Strengthening of A2024 alloy by high-pressure torsion and subsequent aging, Mater. Sci. Eng. A 704 (2017) 112–118.
[63] K. Edalati, H. Shao, H. Emami, H. Iwaoka, E. Akiba, Z. Horita, Activation of titanium-vanadium alloy for hydrogen storage by introduction of nanograins and edge dislocations using high-pressure torsion, Int. J. Hydrogen Energy 41 (2016) 8917–8924.
[64] M. Isika, M. Niinomi, K. Cho, M. Nakai, H. Liu, H. Yilmazer, Z. Horita, S. Sato, T. Narushima, Microstructural evolution and mechanical properties of biomedical Co-Cr-Mo alloy subjected to high-pressure torsion, J. Mech. Behav. Biomed. Mater. 59 (2016) 226–235.
[65] M. Isik, M. Niinomi, H. Liu, K. Cho, M. Nakai, Z. Horita, S. Sato, T. Narushima, H. Yilmazer, M. Nagasako, Grain refinement mechanism and evolution of dislocation structure of Co-Cr-Mo alloy subjected to high-pressure torsion, Mater. Trans. A 57 (2016) 1109–1118.
[66] T. Hongo, K. Edalati, H. Iwaoka, M. Arita, J. Matsuda, E. Akiba, Z. Horita, High-pressure torsion of palladium: hydrogen-induced softening and plasticity in ultrafine grains and hydrogen-induced hardening and embrittlement in coarse grains, Mater. Sci. Eng. A 618 (2014) 1–8.
[67] K. Edalati, K. Imamura, T. Kiss, Z. Horita, Equal-channel angular pressing and high-pressure torsion of pure copper: evolution of electrical conductivity and hardness with strain, Mater. Trans. 53 (2012) 123–127.
[68] A. Hanna, H. Azzeddine, R. Lachha, T. Baudin, A.-L. Helbert, F. Brisset, Y. Huang, D. Bradai, T.G. Langdon, Evaluating the textural and mechanical properties of an Mg-Dy alloy processed by high-pressure torsion, J. Alloy. Compd. 778 (2019) 61–71.
[69] Y.I. Bourezg, H. Azzeddine, T. Baudin, A.-L. Helbert, Y. Huang, D. Bradai, T.G. Langdon, Texture and microhardness of Mg-Rare Earth (Nd and Ce) alloys processed by high-pressure torsion, Mater. Sci. Eng. A 724 (2018) 477–485.
[70] P. Bazarnik, Y. Huang, M. Lewandowska, T.G. Langdon, Enhanced grain refinement and microhardness by hybrid processing using hydrostatic extrusion and high-pressure torsion, Mater. Sci. Eng. A 712 (2018) 513–520.
[71] D.M.M. Cardona, J. Wongsa-Ngam, H. Jimenez, T.G. Langdon, Effects on hardness and microstructure of AISI 1020 low-carbon steel processed by high-pressure torsion, J. Mater. Res. Technol. 6 (2017) 355–360.
[72] S.A. Torbati-Sarraf, S. Sabbaghianrad, R.B. Figueiredo, T.G. Langdon, Orientation imaging microscopy and microhardness in a ZK60 magnesium alloy processed by high-pressure torsion, J. Alloy. Compd. 712 (2017) 185–193.
[73] M. Diez, H.-E. Kim, V. Serebryany, S. Dobatkin, Y. Estrin, Improving the mechanical properties of pure magnesium by three-roll planetary milling, Mater. Sci. Eng. A 612 (2014) 287–292.
[74] E.A. Lukyanova, N.S. Martynenko, I. Shakhova, A.N. Belyakov, L.L. Rokhlin, S.V. Dobatkin, Y.Z. Estrin, Strengthening of age-hardenable WE43 magnesium alloy processed by high pressure torsion, Mater. Lett. 170 (2016) 5–9.
[75] N.S. Martynenko, E.A. Luk'yanova, M.M. Morozov, V.S. Yusupov, S.V. Dobatkin, Y.Z. Estrin, A study of the structure, mechanical properties and corrosion resistance of magnesium alloy WE43 after rotary swaging, Metal Sci. Heat Treat. 60 (2018) 253–258.
[76] C.C. Koch, T.G. Langdon, E.J. Lavernia, Bulk nanostructured materials, Metal. Mater. Trans. A 48 (2017) 5181–5199.
[77] A.A. Mazilkin, B.B. Straumal, M.V. Borodachenkova, R.Z. Valiev, O.A. Kogtenkova, B. Baretzky, Gradual softening of Al–Zn alloys during high pressure torsion, Mater. Lett. 84 (2012) 63–65.
[78] X. Sauvage, M.Yu. Murashkin, B.B. Straumal, E. Bobruk, R.Z. Valiev, Ultrafine grained structures resulting from SPD-induced phase transformation in Al-Zn alloys, Adv. Eng. Mater. 17 (2015) 1821–1827.
[79] V.D. Sitdikov, P.S. Chizhov, M.Yu. Murashkin, R.Z. Valiev, Ultrafine grained structures resulting from SPD-induced phase transformation in Al-Zn alloys, Rev. Adv. Mat. Sci. 47 (2016) 59–65.
[80] G. Martin, Phase stability under irradiation: Ballistic effects, Phys. Rev. B 30 (1984) 1424–1436.
[81] W. Guo, J. Yao, E.A. Jägle, P.-P. Choi, M. Herbig, J.M. Schneider, D. Raabe, Deformation induced alloying in crystalline-metallic glass nano-composites, Mater. Sci. Eng. A 628 (2015) 269–280.
[82] W. Guo, E.A. Jägle, P.-P. Choi, J. Yao, A. Kostka, J.M. Schneider, D. Raabe, Shear-induced mixing governs codeformation of crystalline-amorphous nanolaminates, Phys. Rev. Lett. 113 (2014) 035501.
[83] W. Guo, Y. Meng, X. Zhang, V. Bedekar, H. Bei, S. Hyde, Q. Guo, G.B. Thompson, R. Shivpuri, J. Zuo, J.D. Poplawsky, Extremely hard amorphous-crystalline hybrid steel surface producedby deformation induced cementite amorphization, Acta Mater. 152 (2018) 107–118.
[84] B.B. Straumal, A.R. Kilmametov, A.A. Mazilkin, A.S. Gornakova, O.B. Fabrichnaya, M.J. Kriegel, D. Rafaja, M.F. Bulatov, A.N. Nekrasov, B. Baretzky, The formation of the ω phase in the titanium-iron system under shear deformation, JETP Lett. 111 (2020), doi: 10.1134/S0021364020100033.
[85] A.M. Glezer, R.V. Sundeev, A.V. Shalimova, Phase transformations "amorphyzation ↔ crystallization" in metallic materials induced by severe plastic deformation, Rev. Adv. Mater. Sci. 54 (2018) 93–105.
[86] B.B. Straumal, A.R. Kilmametov, Yu.O. Kucheev, K.I. Kolesnikova, A. Korneva, P. Zięba, B. Baretzky, Transformations of Hume-Rothery phases under the action of high pressure torsion, JETP Lett. 100 (2014) 376–379.
[87] S. Fujikawa, K.I. Hirano, Bulk self diffusion in copper, in: J.I. Takamura, M. Doyama, M. Kiritani (Eds.), Proc. of Yamada Vth Conf. On Point Defects, Defect Interactions in Metals, Univ. of Tokyo Press, Tokyo, 1982, pp. 554–558.
[88] H. Mehrer (Ed.), Diffusion in Solid Metals and Alloys, Landolt-Börnstein New Series, Gr III, 26, Springer-Verlag, Berlin, 1990, p. 187.
[89] B.B. Straumal, L.M. Klinger, L.S. Shvindlerman, The influence of pressure on indium diffusion along single tin-germanium interphase boundaries, Scr. Metall. 17 (1983) 275–279.
[90] D.A. Molodov, B.B. Straumal, L.S. Shvindlerman, The effect of pressure on migration of the [001]tilt grain boundaries in the tin bicrystals, Scr. Metall. 18 (1984) 207–211.
[91] D.A. Molodov, J. Swiderski, G. Gottstein, W. Lojkowski, L.S. Shvindlerman, Effect of pressure on grain boundary migration in aluminium bicrystals, Acta Metall. Mater. 42 (1994) pp. 3997–3407.
[92] B.B. Straumal, A.R. Kilmametov, Yu.O. Kucheev, L. Kurmanaeva, Yu. Ivanisenko, B. Baretzky, A. Korneva, P. Zięba, D.A. Molodov, Phase transitions during high pressure torsion of Cu-Co alloys, Mater. Lett. 118 (2014) 111–114.
[93] C.A. Mackliet, Diffusion of iron, cobalt, and nickel in single crystals of pure copper, Phys. Rev. 109 (1958) 1964–1970.
[94] V.A. Gorbachev, S.M. Klotsman, Ya.A. Rabovskiy, V.K. Talinskiy, A.N. Timofeyev, Diffusion of tin and antimony in copper single crystals, Phys. Met. Metallogr. 35 (4) (1973) 226–230.
[95] A.A. Mazilkin, B.B. Straumal, A.R. Kilmametov, T. Boll, B. Baretzky, O.A. Kogtenkova, A. Korneva, P. Zięba, Competition for impurity atoms between defects and solid solution during high pressure torsion, Scripta Mater 173 (2019) 46–50.
[96] D. Gaertner, G. Wilde, S.V. Divinski, Grain boundary diffusion and segregation of ^{57}Co in high-purity copper: Radiotracer measurements in B- and C-type diffusion regimes, Acta Mater. 127 (2017) 407–415.
[97] S.V. Divinski, H. Edelhoff, S. Prokofjev, Diffusion and segregation of silver in copper Σ5(310) grain boundary, Phys. Rev. B 85 (2012) 144104.
[98] H. Mehrer (Ed.), Diffusion in Solid Metals and Alloys, Landolt-Börnstein New Series, Gr III, 26, Springer-Verlag, Berlin, 1990.
[99] P. Lejček, Grain Boundary Segregation in Metals, Springer Series in Materas Science, 136, Springer-Verlag, Berlin, 2010.
[100] M. Menyhard, Silver grain boundary segregation in copper, Mater. Sci. Forum 126 (1993) 205–208.
[101] Z. Erdélyi, Ch. Girardeaux, G.A. Langer, D.L. Beke, A. Rolland, J. Bernardini, Determination of grain-boundary diffusion of Ag in nanocrystalline Cu by the Hwang-Balluffi method, J. Appl. Phys. 89 (2001) 3971–3975.
[102] S.V. Divinski, M. Lohmann, Chr. Herzig, Ag grain boundary diffusion and segregation in Cu: measurements in the types B and C diffusion regimes, Acta Mater. 49 (2001) 249–261.
[103] S.V. Divinski, C. Herzig, Radiotracer investigation of diffusion, segregation and wetting phenomena in grain boundaries, J. Mater. Sci. 43 (2008) 3900–3907.
[104] S.V. Divinski, M. Lohmann, Chr. Herzig, Grain boundary diffusion and linear and non-linear segregation of Ag in Cu, Interface Sci. 11 (2003) 21–31.
[105] H. Edelhoff, S.V. Divinski, S. Prokofjev, The C-regime measurements of grain boundary diffusion of silver in copper Sigma 5 (310) bicrystal, Scr. Mater. 64 (2011) 374–377.
[106] A. Kwiatkowski da Silva, G. Leyson, M. Kuzmina, D. Ponge, M. Herbig, S. Sandlöbes, B. Gault, J. Neugebauer, D. Raabe, Confined chemical and structural states at dislocations in Fe-9wt%Mn steels: a correlative TEM-atom probe study combined with multiscale modelling, Acta Mater. 124 (2017) 305–315.
[107] S.J. Dillon, K. Tai, S. Chen, The importance of grain boundary complexions in affecting physical properties of polycrystals, Curr. Opin. Solid State Mater. Sci. 20 (2016) 324–335.
[108] M. Kuzmina, M. Herbig, D. Ponge, S. Sandlöbes, D. Raabe, Linear complexions: confined chemical and structural states at dislocations, Science 349 (2015) 1080–1083.
[109] L.-S. Chang, B.B. Straumal, E. Rabkin, W. Gust, F. Sommer, The solidus line of the Cu-Bi phase diagram, J. Phase Equl. 18 (2) (1997) 128–135.
[110] L.-S. Chang, E. Rabkin, B. Straumal, P. Lejcek, S. Hofmann, W. Gust, Temperature dependence of the grain boundary segregation of Bi in Cu polycrystals, Scr. Mater. 37 (6) (1997) 729–735.
[111] L.-S. Chang, E. Rabkin, B.B. Straumal, S. Hoffmann, B. Baretzky, W. Gust, Grain boundary segregation in the Cu-Bi system, Defect Differ. Forum 156 (1998) 135–146.

[112] N. Lugo, N. Llorca, J.M. Cabrera, Z. Horita, Microstructures and mechanical properties of pure copper deformed severely by equal-channel angular pressing and high pressure torsion, Mater. Sci. Eng. A 477 (2008) 366–371.
[113] J. Čížek, M. Janeček, O. Srba, R. Kuzel, Z. Barnovska, I. Prochazka, S. Dobatkin, Evolution of defects in copper deformed by high-pressure torsion, Acta Mater. 59 (2011) 2322–2329.
[114] F. Ernst, M.W. Finnis, A. Koch, C. Schmidt, B. Straumal, W. Gust, Structure and energy of twin boundaries in copper, Z. Metallk. 87 (1996) 911–922.
[115] H. Grimmer, W. Bollmann, D.T. Warrington, Coincidence-site lattices and complete pattern-shift in cubic crystals, Acta Cryst. A 30 (1974) 197–207.
[116] B.B. Straumal, S.A. Polyakov, E. Bischoff, W. Gust, E.J. Mittemeijer, Faceting of $\Sigma 3$ and Σ 9 grain boundaries in copper, Interface Sci. 9 (2001) 287–292.
[117] B.B. Straumal, L.S. Shvindlerman, Regions of existence of special and non-special grain boundaries, Acta Metall. 33 (1985) 1735–1749.
[118] C. Minkwitz, Chr. Herzig, E. Rabkin, W. Gust, The inclination dependence of gold tracer diffusion along a $\Sigma 3$ twin grain boundary in copper, Acta Mater. 47 (1999) 1231–1239.
[119] A.N. Aleshin, S.I. Prokofiev, L.S. Shvindlerman, Evidence of structure transformation in Σ = 5 near-coincidence grain boundaries, Scr. Metall. 19 (1985) 1135–1140.
[120] T.E. Hsieh, R.W. Balluffi, Observations of roughening/de-faceting phase transitions in grain boundaries, Acta Met. 37 (1989) 2133–2139.
[121] M.J. Kim, Y.K. Cho, D.Y. Yoon, Facet–defacet transition of grain boundaries in alumina, J. Am. Ceram. Soc. 87 (2004) 455–460.
[122] K.O. Keshishev, A.Ya. Parshin, A.V. Babkin, Crystallization waves in ^{4}He, Sov. Phys. JETP 53 (1981) 362–369.
[123] C. Rottman, M. Wortis, Exact equilibrium crystal shapes at nonzero temperature in two dimensions, Phys. Rev. B 24 (1981) 6274–6277.
[124] C. Rottman, M. Wortis, Equilibrium crystal shapes for lattice models with nearest-and next-nearest-neighbor interactions, Phys. Rev. B 29 (1984) 328–339.
[125] B.B. Straumal, O.A. Kogtenkova, A.S. Gornakova, V.G. Sursaeva, B. Baretzky, Review: grain boundary faceting-roughening phenomena, J. Mater. Sci. 51 (2016) 382–404.
[126] B.B. Straumal, S.A. Polyakov, E.J. Mittemeijer, Temperature influence on the faceting of $\Sigma 3$ and $\Sigma 9$ grain boundaries in Cu, Acta Mater. 54 (2006) 167–172.
[127] A. Kosinova, B.B. Straumal, A.R. Kilmametov, E. Rabkin, The effect of bismuth on microstructure evolution of ultrafine grained copper, Mater. Lett. 199 (2017) 156–159.
[128] Y. Qi, A. Kosinova, A.R. Kilmametov, B.B. Straumal, E. Rabkin, Generation and healing of porosity in high purity copper by high-pressure torsion, Mater. Charact. 145 (2018) 1–9.
[129] A. Kosinova, B. Straumal, A. Kilmametov, P. Straumal, M. Bulatov, E. Rabkin, Faceting of twin grain boundaries in high-purity copper subjected to high pressure torsion, Adv. Eng. Mater. 21 (2019) 1900589 (8pp).
[130] B. Oberdorfer, E.-M. Steyskal, W. Sprengel, W. Puff, M. Zehetbauer, R. Pippan, R. Wuerschum, In situ probing of fast defect annealing in Cu and Ni with a high-intensity positron beam, Phys. Rev. Lett. 105 (2010) 146101.
[131] B. Oberdorfer, D. Setman, E.-M. Steyskal, A. Hohenwarter, W. Sprengel, M. Zehetbauer, R. Pippan, R. Würschum, Grain boundary excess volume and defect annealing of copper after high-pressure torsion, Acta Mater. 68 (2014) 189–195.
[132] J. Čízek, O. Melikhova, Z. Barnovská, I. Procházka, R.K. Islamgaliev, Vacancy clusters in ultra fine grained metals prepared by severe plastic deformation, J. Phys. Conf. Ser. 443 (2013) 012008.